This is a repository copy of *The core normal Type Ia supernova 2019np – an overall spherical explosion with an aspherical surface layer and an aspherical 56Ni core*.

White Rose Research Online URL for this paper:
https://eprints.whiterose.ac.uk/199597/

Version: Published Version

Article:
Hoeflich, P., Yang, Y. orcid.org/0000-0002-6535-8500, Baade, D. et al. (10 more authors) (2023) The core normal Type Ia supernova 2019np – an overall spherical explosion with an aspherical surface layer and an aspherical 56Ni core. Monthly Notices of the Royal Astronomical Society, 520 (1). pp. 560-582. ISSN 0035-8711

https://doi.org/10.1093/mnras/stad172

This article has been accepted for publication in Monthly Notices of the Royal Astronomical Society ©: 2023 The Author(s) Published by Oxford University Press on behalf of the Royal Astronomical Society. All rights reserved.

Reuse
Items deposited in White Rose Research Online are protected by copyright, with all rights reserved unless indicated otherwise. They may be downloaded and/or printed for private study, or other acts as permitted by national copyright laws. The publisher or other rights holders may allow further reproduction and re-use of the full text version. This is indicated by the licence information on the White Rose Research Online record for the item.

Takedown
If you consider content in White Rose Research Online to be in breach of UK law, please notify us by emailing eprints@whiterose.ac.uk including the URL of the record and the reason for the withdrawal request.

eprints@whiterose.ac.uk
https://eprints.whiterose.ac.uk/

Monthly Notices of the ROYAL ASTRONOMICAL SOCIETY

MNRAS **520,** 560–582 (2023) https://doi.org/10.1093/mnras/stad172
Advance Access publication 2023 January 16

The core normal Type Ia supernova 2019np – an overall spherical explosion with an aspherical surface layer and an aspherical ^{56}Ni core

Peter Hoeflich,[1★†‡] Yi Yang(杨轶),[2,3★] Dietrich Baade,[4★] Aleksandar Cikota,[5,6] Justyn R. Maund,[7] Divya Mishra,[8] Ferdinando Patat,[4] Kishore C. Patra,[2] Lifan Wang,[8] J. Craig Wheeler,[9] Alexei V. Filippenko,[2] Avishay Gal-Yam[10] and Steven Schulze[11]

[1]*Department of Physics, Florida State University, Tallahassee, FL 32306, USA*
[2]*Department of Astronomy, University of California, Berkeley, CA 94720, USA*
[3]*Department of Particle Physics and Astrophysics, Weizmann Institute of Science, Rehovot 76100, Israel*
[4]*European Organisation for Astronomical Research in the Southern Hemisphere (ESO), Karl-Schwarzschild-Str. 2, D-85748 Garching b. München, Germany*
[5]*European Organisation for Astronomical Research in the Southern Hemisphere (ESO), Alonso de Cordova 3107, Vitacura, Casilla 19001, Santiago de Chile, Chile*
[6]*Gemini Observatory/NSF's NOIRLab, Casilla 603, La Serena, Chile*
[7]*Department of Physics and Astronomy, University of Sheffield, Hicks Building, Hounsfield Road, Sheffield S3 7RH, UK*
[8]*George P. and Cynthia Woods Mitchell Institute for Fundamental Physics & Astronomy, Texas A&M University, 4242 TAMU, College Station, TX 77843, USA*
[9]*Department of Astronomy, University of Texas, Austin, TX 78712, USA*
[10]*Department of Particle Physics and Astrophysics, Weizmann Institute of Science, 76100 Rehovot, Israel*
[11]*The Oskar Klein Centre, Department of Astronomy and Department of Physics, Stockholm University, AlbaNova, SE-106 91 Stockholm, Sweden*

Accepted 2023 January 11. Received 2023 January 11; in original form 2022 October 28

ABSTRACT

Optical spectropolarimetry of the normal thermonuclear supernova (SN) 2019np from −14.5 to +14.5 d relative to *B*-band maximum detected an intrinsic continuum polarization ($p^{\rm cont}$) of 0.21 ± 0.09 per cent at the first epoch. Between days −11.5 and +0.5, $p^{\rm cont}$ remained ∼0 and by day +14.5 was again significant at 0.19 ± 0.10 per cent. Not considering the first epoch, the dominant axis of Si II λ6355 was roughly constant staying close the continuum until both rotated in opposite directions on day +14.5. Detailed radiation-hydrodynamical simulations produce a very steep density slope in the outermost ejecta so that the low first-epoch $p^{\rm cont} \approx 0.2$ per cent nevertheless suggests a separate structure with an axis ratio ∼2 in the outer carbon-rich (3.5–4) × 10^{-3} $M_\odot$. Large-amplitude fluctuations in the polarization profiles and a flocculent appearance of the polar diagram for the Ca II near-infrared triplet (NIR3) may be related by a common origin. The temporal evolution of the polarization spectra agrees with an off-centre delayed detonation. The late-time increase in polarization and the possible change in position angle are also consistent with an aspherical ^{56}Ni core. The $p^{\rm cont}$ and the absorptions due to Si II λ6355 and Ca II NIR3 form in the same region of the extended photosphere, with an interplay between line occultation and thermalization producing *p*. Small-scale polarization features may be due to small-scale structures, but many could be related to atomic patterns of the quasi-continuum; they hardly have an equivalent in the total-flux spectra. We compare SN 2019np to other SNe and develop future objectives and strategies for SN Ia spectropolarimetry.

Key words: polarization – supernovae: individual: (SN, 2019np).

1 INTRODUCTION

Various models of Type Ia supernova (SN) explosions predict photometric and spectroscopic evolution that reproduce observations adequately but not uniquely (Alsabti & Murdin 2017), so it is difficult to judge models merely by their power in matching light curves and total-flux spectra. However, they predict different explosion geometries of the progenitor white dwarf (WD), which can be diagnosed with polarimetry (Hoeflich et al. 2021). Polarized optical flux from SNe can be caused by departures from spherical symmetry of the global ejecta structure or by chemical 'clumps' with different line opacities that block portions of the photosphere (Wang & Wheeler 2008; Patat 2017). Both schemes can be understood as an incomplete cancellation of the electric vectors integrated over the photosphere as seen by the observer. Optical polarimetry probes the geometric properties of the SN explosion and the structure of the SN ejecta, without spatially resolving the source. A wavelength-independent continuum polarization would arise from Thomson scattering of free electrons with a globally aspherical distribution. In addition or alternatively, it may be caused by energy input that is spatially offset from the centre of mass (Hoeflich, Khokhlov &

★ E-mail: phoeflich77@gmail.com (PH); yiyangtamu@gmail.com (YY); dbaade@eso.org (DB)
† Bengier-Winslow-Robertson Fellow.
‡ Nagaraj-Noll-Otellini Graduate Fellow.

© 2023 The Author(s)
Published by Oxford University Press on behalf of Royal Astronomical Society

Downloaded from https://academic.oup.com/mnras/article/520/1/560/6988185 by University of Sheffield user on 26 May 2023

Wheeler 1995; Livne 1999; Kasen et al. 2003; Höflich et al. 2006a). Polarized spectral features can be induced in the SN ejecta by chemically uneven blocking within the photosphere and by frequency variations of the associated line opacities in the thermalization depth.

Any early polarization signal from thermonuclear explosions offers a critical test of the nature of the progenitor systems of Type Ia SNe. For example, large deviations from global sphericity in the density distribution and chemical abundances of the ejecta are predicted for explosions triggered by the dynamical merger of a double WD binary (Pakmor et al. 2012; Bulla et al. 2016a). The resulting polarization is expected to be significant both in the continuum and across various spectral lines. The continuum polarization can be as high as $\gtrsim$0.5–1 per cent at $\sim$1 week after the explosion if observed out of the orbital plane (Bulla et al. 2016a). By contrast, an almost spherical density distribution and a moderate degree of chemical inhomogeneity are predicted by delayed-detonation models (Höflich et al. 2006a; Pakmor et al. 2012, 2013; Moll et al. 2014; Raskin et al. 2014). A continuum polarization near zero as well as modest ($\lesssim$ 1 per cent) signals across major spectral features were also predicted by specific multidimensional models for both a selected delayed-detonation and a sub-Chandrasekhar-mass ($M_{\rm Ch}$) model (Bulla et al. 2016b).

Polarized spectral lines indicate geometric deviations from spherical symmetry of the associated elements. Chemical inhomogeneities are imprinted by the propagation of the burning front. Delayed-detonation models predict an initial subsonic deflagration resulting in turbulence and gravitational compression. As the burning front travels outward, the flame transforms into a supersonic detonation because of Rayleigh–Taylor instability at the interface between unburned and burned material (Khokhlov 1991). Layers of intermediate-mass elements (IMEs; i.e. from Si to Ca) are then produced at the front of the detonation wave. At any given epoch, the polarization spectrum samples the geometric information of the ejecta that intersect the photosphere. As the ejecta expand over time, the electron density decreases and the photosphere recedes into deeper layers of the ejecta in mass and velocity. Multiepoch spectropolarimetry tomographically maps out the distribution of various elements.

More recent early-time observations have also found low continuum polarization in other normal Type Ia SNe namely SN 2018gv (day $-$13.6; Yang et al. 2020) and SN 2019ein (day $-$10.9; Patra et al. 2022). SN 2019ein displayed one of the highest expansion velocities at early phases as inferred from the absorption minimum of the Si II λ6355 line ($\sim$24 000 km s^{-1} at 14 d before photometric *B*-band maximum; Pellegrino et al. 2020). The low continuum polarization on day $-$10.9 indicates a low degree of asphericity at this phase, strengthening the existing evidence that the explosions of Type Ia SNe maintain a high degree of sphericity from their early phases. The spectropolarimetry of SN 2018gv on day $-$13.6 was the earliest such measurement at its time for any Type Ia SN. The 0.2 $\pm$ 0.13 per cent continuum polarization 5 d after the explosion (based on phase estimates from the early light curve) suggests that the photosphere was moderately aspherical with an axis ratio of 1.1–1.3.[1] However, even at this early phase, the geometry of the outermost $\sim10^{-3}$ to $\sim10^{-2}$ $M_{\rm WD}$ of SN 2018gv still remained observationally unconstrained. The polarization is also sensitive to the rapidly changing density structure in the outer layers, which intersect the photosphere in the first few days (Hoeflich et al. 2017).

SN 2019np was discovered at 2019-01-09 15:58 (UT dates are used throughout this paper) with a 0.5 m telescope at a clear-band magnitude of 17.8 (Itagaki 2019). Rapid spectroscopic follow-up observations were carried out as early as $\sim$1 d after the discovery (Burke et al. 2019; Kilpatrick & Foley 2019; Wu et al. 2019). Spectral cross-correlations with the 'Supernova Identification' (SNID; Blondin & Tonry 2007) and the 'Superfit' (Howell et al. 2005) codes suggest that SN 2019np is a Type Ia SN discovered $\sim$2 weeks before maximum light. From the photometry by Burke et al. (2022), we derived that SN 2019np reached its peak *B*-band magnitude at MJD 58509.72 $\pm$ 0.06 $\pm$ 0.51 (see Appendix A), where the two uncertainties represent the statistical and the systematic error, respectively. This estimate is consistent with the respective values of 58510.2 $\pm$ 0.8 and 58509.64 $\pm$ 0.06 reported by Sai et al. (2022) and Burke et al. (2022). All phases used throughout the present paper are given relative to the *B*-band maximum light at MJD 58509.72 (2019-01-26.72). A comprehensive study of the SN by Sai et al. (2022) concluded that its photometric and spectroscopic properties were similar to those of other normal Type Ia SNe.

Sai et al. (2022) detected a $\lesssim$5 per cent excess in the early bolometric flux evolution of SN 2019np compared to radiative diffusion models (Arnett 1982; Chatzopoulos, Wheeler & Vinko 2012), hinting at additional energy input compared to the radioactive decay of a Ni core. They suggested that the blue and relatively fast-rising early light curves of SN 2019np are best fitted with the mixing of ^{56}Ni from the inner to the outer layers of the SN ejecta (Piro & Morozova 2016). The rise time of SN 2019np is not compatible with models that predict an early interaction between the SN ejecta and any ambient circumstellar matter (CSM) or a companion star (Kasen 2010). Moreover, the colour evolution of SN 2019np is inconsistent with that predicted for a progenitor WD below $M_{\rm Ch}$ and surrounded by a thin helium shell as discussed in Sections 4.4 and 6.1. In this 'double-detonation' or 'He-shell detonation' picture, an initial detonation is triggered in the surface He shell, sending a shock wave to the inner region of the C/O WD. The shock generates compression heat and subsequently triggers the second detonation that ignites the WD (Woosley, Weaver & Taam 1980; Nomoto 1982a,b; Livne 1990; Woosley & Weaver 1994; Hoeflich & Khokhlov 1996; Kromer et al. 2010). Burke et al. (2022) also suggested an excess in the early flux evolution of SN 2019np, which may have been too weak to have been caused by an interaction between the ejecta and a companion. Interaction with any CSM is an additional possibility.

This study presents five epochs of optical spectropolarimetry of SN 2019np from $t \approx -14.5$ to $+14.5$ d and interpretations based on detailed radiation-hydrodynamic simulations. The paper is organized as follows. In Section 2, we outline the spectropolarimetric observations and the data-reduction procedure. The polarization properties of SN 2019np are discussed in Section 3. The analysis of these properties with hydrodynamic models is carried out in Section 4. We summarize our conclusions in Section 5, and develop a comprehensive appraisal of the potential of spectropolarimetry for the understanding of Type Ia SNe in Section 6.

2 SPECTROPOLARIMETRY OF SN 2019NP

Spectropolarimetry of SN 2019np was conducted with the FOcal Reducer and low dispersion Spectrograph 2 (FORS2; Appenzeller

[1]Throughout the paper, the term equatorial plane is defined by planes through the centre, $\vec{n}\vec{x} = 0$, $\vec{x}$ spanning the plane with the symmetry axis of a rotationally symmetric ellipsoid as the orthogonal vector $\vec{n}$, or $\vec{n}$ being a line through the centre of the WD and the location of an off-centre energy source (Höflich 1995c). The two so defined planes may be different (Section 4).

Downloaded from https://academic.oup.com/mnras/article/520/1/560/6988185 by University of Sheffield user on 26 May 2023

Table 1. Log of spectropolarimetry of SN 2019np.

Epoch	Object	MJD	Date (UT)	Phase[a] (d)	Exposure (s)	Grism / Resol. Power	Airmass Range
1[b]	SN 2019np	58495.270	2019-01-12 06:30	−14.5	4 × 550	300V/440	1.84–1.73
		58495.298	2019-01-12 07:10		4 × 550	300V/440	1.73–1.70
2	SN 2019np	58498.302	2019-01-15 07:14	−11.4	4 × 600	300V/440	1.71–1.70
3	SN 2019np	58503.305	2019-01-20 07:18	−6.4	4 × 210	300V/440	1.70–1.71
	HD 93621[c]	58503.322	2019-01-20 07:43	–	1 × 0.51	300V/440	2.13
4	SN 2019np	58510.272	2019-01-27 06:31	+0.5	4 × 360	300V/440	1.71–1.70
5	SN 2019np	58524.188	2019-02-10 04:31	+14.5	4 × 360	300V/440	1.71–1.70

Notes. [a]Relative to the estimated peak on MJD 58509.7/UT 2019-01-26.7; MJD and date are given as the start time of the CCD exposure.
[b]Epoch 1 observation consists of two sets of exposures at four half-wave plate angles.
[c]Flux standard, observed at a half-wave plate angle of 0°.

et al. 1998) on Unit Telescope 1 (UT1, Antu) of the ESO Very Large Telescope (VLT). The Polarimetric Multi-Object Spectroscopy (PMOS) mode was used for all science observations. A complete set of spectropolarimetry consists of four exposures at retarder-plate angles of 0, 22.5, 45, and 67.5 deg. The 300V grism and a 1 arcsec-wide slit were selected for all observations. The order-sorting filter GG435 was in place, which has a cut-on at ∼4350 Å to prevent shorter wavelength second-order contamination. This configuration provides a spectral resolving power of $R \approx 440$ at a central wavelength of 5849 Å, corresponding to a resolution-element size of ∼13 Å (or ∼670 km s^{-1}) according to the VLT FORS2 user manual (Anderson 2018).

Observations were obtained at five epochs: (in the format day/UT) −14.5/2019-01-12, −11.4/2019-01-15, −6.4/2019-01-20, +0.5/2019-01-27, and +14.5/2019-02-10. At the first epoch, the total 4 × 1100 s integration time was split into two sets of exposures to reduce the impact of cosmic rays. The two loops were carried out at relatively large and different airmasses, from 1.84 to 1.73 and from 1.73 to 1.70. We conducted a consistency check of the two measurement sets and found that the Stokes parameters derived for the two loops agree within their 1σ uncertainties over the entire wavelength range after rebinning the data to larger resolution elements (e.g. 30 Å and 40 Å bin sizes). We thus combined the two data sets by taking the mean value of the spectra obtained at each retarder-plate angle. Relative-flux calibration was based on the flux standard star HD 93621 observed at a half-wave plate angle 0 deg near epoch 3. The airmass of the flux standard was chosen to be comparable to that of the spectropolarimetry of SN 2019np. A log of the VLT spectropolarimety is presented in Table 1.

After bias and flat-field corrections, the ordinary (o) and extraordinary (e) beams in each two-dimensional spectral image were extracted following standard routines within IRAF[2] (Tody 1986, 1993). A typical root mean square (RMS) accuracy of ∼0.20 Å was achieved in the wavelength calibrations. Stokes parameters were then derived using our own routines based on the prescriptions in Patat & Romaniello (2006) and Maund et al. (2007), which also correct the bias due to the non-negativity of the polarization degree. The observed polarization degree and position angle ($p_{\rm obs}$, $\rm PA_{obs}$) and the true values after bias correction (p, PA) can be written as

$$p_{\rm obs} = \sqrt{Q^2 + U^2},\ p = \left(p_{\rm obs} - \frac{\sigma_p^2}{p_{\rm obs}}\right) \times h(p_{\rm obs} - \sigma_p);$$
$$\rm PA_{obs} = \frac{1}{2}\arctan\left(\frac{U}{Q}\right),\ \text{and PA} = PA_{obs}. \quad (1)$$

Here, Q and U are the intensity (I)-normalized Stokes parameters. The correction for the polarization bias is based on equations in Simmons & Stewart (1985) and Wang, Wheeler & Höflich (1997), where σ_p and h denote the 1σ uncertainty in $p_{\rm obs}$ and the Heaviside step function, respectively. The brackets are properly set as in Cikota et al. (2019).

A ≲0.1 per cent instrumental polarization was also corrected following the procedure discussed by Cikota et al. (2017). More details of the reduction of FORS2 spectropolarimetry can be found in the FORS2 Spectropolarimetry Cookbook and Reflex Tutorial,[3] as well as in Cikota et al. (2017) and Yang et al. (2020).

3 POLARIMETRIC PROPERTIES OF SN 2019NP

The spectropolarimetry of SN 2019np obtained on days −14.5, −11.4, −6.4, +0.5, and +14.5 is presented in Figs 1–5, respectively, where the data are not corrected for interstellar polarization (ISP). Polarization spectra are shown together with the associated scaled total-flux spectra (hereafter referred to as simply 'flux spectra'). Both have been transformed to the rest frame.

3.1 Interstellar polarization

Removing the polarization imposed by interstellar dust grains in either the Milky Way or the host galaxy or both is essential for revealing the intrinsic polarization of SNe. This ISP is due to dichroic extinction by non-spherical dust grains aligned by the interstellar magnetic field. Therefore, the entire observed wavelength range of the spectrum is used to determine the overall level of the ISM polarization. As will be shown in Section 4.3, both the overall level and the continuum polarization in a narrow wavelength range plus the spectral features are consistent in our analysis. This provides an argument that the procedure to find the ISM polarization does not suppress an overall net-polarization mimicking overall sphericity. The intrinsic continuum polarization of Type Ia SNe around their

[2]IRAF is distributed by the National Optical Astronomy Observatories, which are operated by the Association of Universities for Research in Astronomy, Inc., under cooperative agreement with the National Science Foundation.

[3]ftp://ftp.eso.org/pub/dfs/pipelines/instruments/fors/fors-pmos-reflex-tutorial-1.3.pdf

Downloaded from https://academic.oup.com/mnras/article/520/1/560/6988185 by University of Sheffield user on 26 May 2023

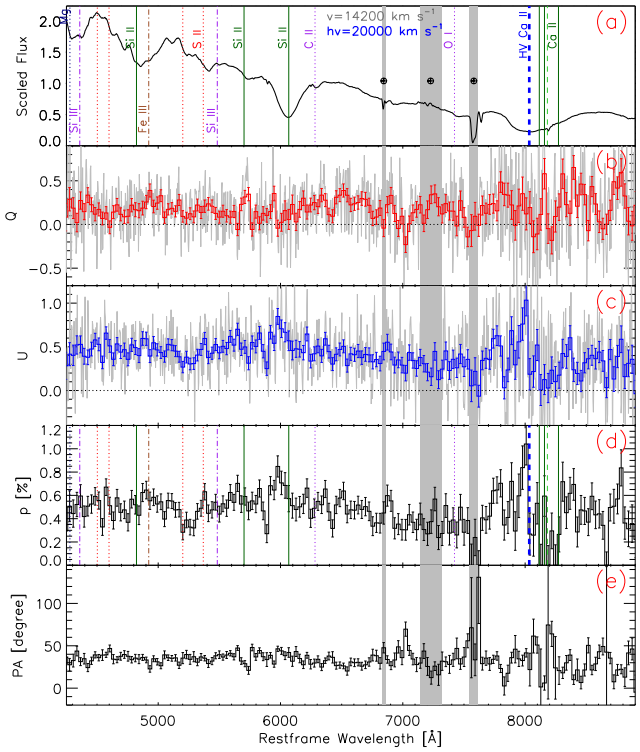

Figure 1. Spectropolarimetry of SN 2019np on day −14.5 (epoch 1) relative to *B*-band maximum light on MJD 58509.7. The five panels (from top to bottom) display (a) the arbitrarily scaled flux spectrum with major spectral features identified and the high-velocity component of Ca II NIR3 labelled 'hv'; (b,c) the normalized Stokes parameters Q and U, respectively; (d) the polarization spectrum (p); and (e) the polarization position angle. Panels (b)–(e) represent the polarimetry before ISP correction. The grey lines in panels (b) and (c) show the data with their original sampling while the heavy lines in panels (b)–(e) use 30 Å bins for clarity. The grey-shaded vertical bands identify regions of telluric contamination.

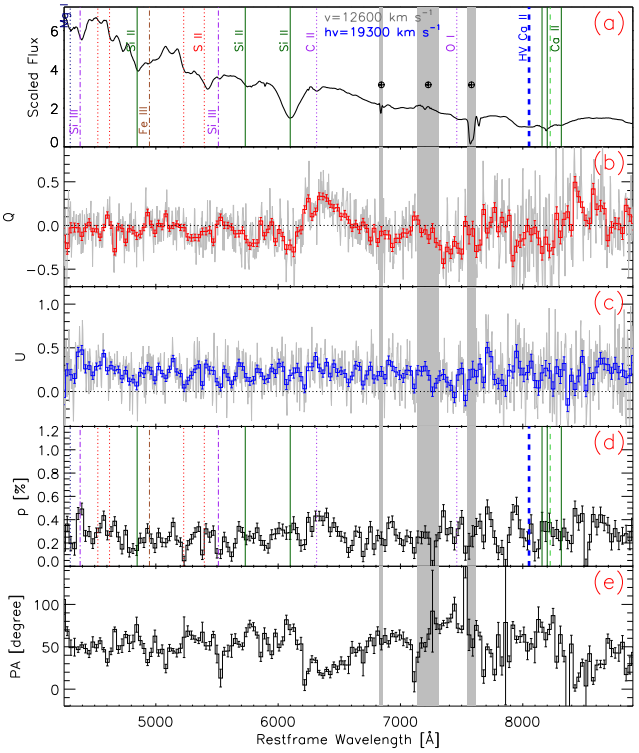

Figure 2. Same as Fig. 1, but for day −11.4 (epoch 2).

peak luminosity is very low ($\lesssim 0.2$ per cent; see e.g. Wang & Wheeler 2008; Patat 2017; Yang et al. 2020). Therefore, we used the spectrum of SN 2019np from day +0.5 as an unpolarized standard. We fitted the Stokes Q, U parameters and the observed degree of polarization, p, using Serkowski's wavelength-dependent law (Serkowski, Mathewson & Ford 1975) as well as a mere constant. In the given low-ISP regime, we found that Serkowski's law failed to yield a satisfactory fit, and the ISP can be characterized by the latter approach, which requires computing the error-weighted mean values of Q and U over suitably selected spectral regions. Using the wavelength range 4400–8900 Å but excluding the telluric features and the strongly polarized Si II λ6355 line and the Ca II near-infrared (NIR) triplet (8500.36 Å, 8544.44 Å, and 8664.52 Å, with a central wavelength of $\lambda_0 \approx 8570$, denoted as Ca II NIR3 hereafter) due to the SN, we estimate the ISP as $(Q_{\rm ISP}, U_{\rm ISP}) = (0.019 \pm 0.121$ per cent, 0.322 ± 0.072 per cent), and $p_{\rm ISP} = 0.343 \pm 0.075$ per cent. These values are well consistent with the ISP derived over the wavelength ranges which are considered to be depolarized due to blanketing by numerous iron absorption lines (see e.g. Howell et al. 2001; Höflich et al. 2006b; Patat et al. 2008; Maund et al. 2013; Patat et al. 2015; Yang et al. 2020). Adopting the Galactic and the host-galaxy reddening of SN 2019np of $E(B-V)_{\rm Gal} = 0.018$ mag and $E(B-V)_{\rm host} = 0.10 \pm 0.03$ mag (Sai et al. 2022), we find the estimated ISP consistent with the empirical upper limit caused by dichroic extinction and established for dust in the Galaxy, $p_{\rm ISP} < 9$ per cent $\times E(B-V)$, following Serkowski et al. (1975).

3.2 Intrinsic continuum polarization

After subtracting the ISP, we determined the continuum polarization of SN 2019np at all epochs from the Stokes parameters over the wavelength range 6400–7000 Å, which is considered to be free of significant polarized spectral features (Patat et al. 2009). The error-weighted mean Stokes parameters within this region are given in Table 2. The uncertainty was estimated by adding the statistical errors and the standard deviation computed from the 30 Å-binned spectra within the chosen wavelength range in quadrature. The continuum polarization within this wavelength interval is consistent with that computed over the entire observed wavelength range after exclusion of the broad, polarized Si II λ6355 and Ca II NIR3 lines.

The intrinsic continuum polarization of SN 2019np on day −14.5 was 0.21 ± 0.09 per cent. After only 3 d, it had dropped to ∼0 by day −11.4 and remained low until the SN reached its peak luminosity. By day +14.5, the continuum polarization had increased to 0.19 ± 0.10 per cent.[4] From the power-law fit of the earliest light curves of SN 2019np, we place the time of first light at $t_0 = -17.92 \pm 0.06$ d, where 0.06 d is only the statistical error (see Appendix A). An additional systematic error of ±0.51 d results from the determination of the time of the peak luminosity. The times of the five epochs of VLT spectropolarimetry relative to this time of the SN explosion are

[4]Note that the time variation in $p^{\rm cont}$ is at a 2σ level. However, the significance of the variation is strongly supported by the change in the dominant axes in the Q–U plane. Moreover, the estimate of the uncertainty in $p^{\rm cont}$ includes real spectral variations in p caused by spectral features (see Sections 3.2, 3.3, and 4.3).

Downloaded from https://academic.oup.com/mnras/article/520/1/560/6988185 by University of Sheffield user on 26 May 2023

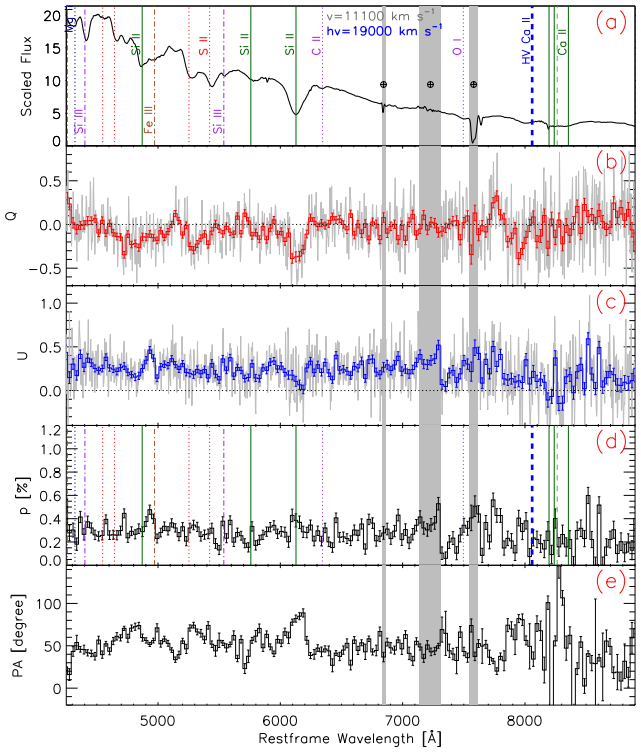

Figure 3. Same as Fig. 1, but for day −6.4 (epoch 3).

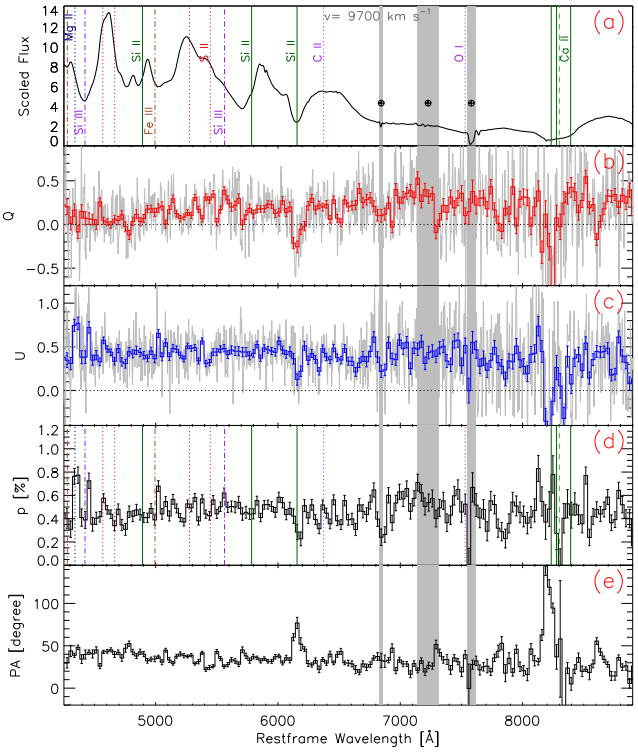

Figure 5. Same as Fig. 1, but for day +14.5 (epoch 5).

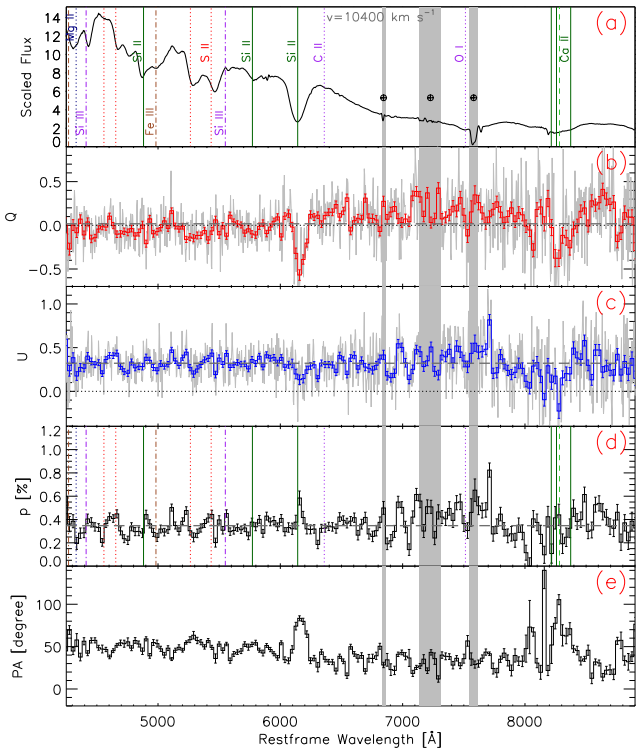

Figure 4. Same as Fig. 1, but for day +0.5 (epoch 4). The estimated ISP level is shown by grey-dashed lines in panels (b)–(d).

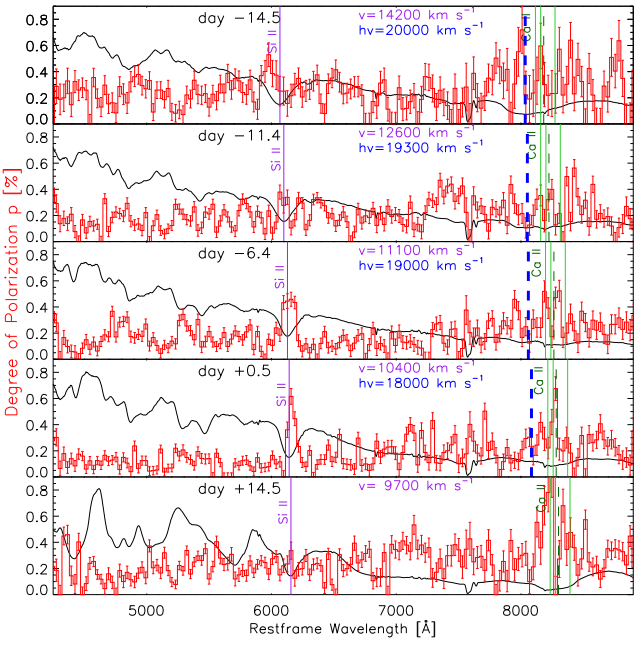

Figure 6. Intrinsic polarization of SN 2019np from days −14.5 to +14.5 as labelled from top to bottom in the subpanels. For each epoch, the degree of polarization is calculated based on ISP-subtracted Stokes Q and U, bias-corrected following equation (1), and presented (red histograms) with 30 Å binning, together with the arbitrarily scaled flux spectrum (black lines). Si II λ6355 and the photospheric component of the Ca II NIR3 features are marked, and their velocities (v) are also given. The high-velocity component of the Ca II NIR3 feature is labelled 'hv.'.

Downloaded from https://academic.oup.com/mnras/article/520/1/560/6988185 by University of Sheffield user on 26 May 2023

Table 2. Values of least-squares fitting parameters on the Q–U plane for SN 2019np.

#Epoch Phase[a]	$Q^{\rm cont}$ $U^{\rm cont}$	$p^{\rm cont}$ (per cent)	α / α^* β / β^*	θ_d / θ_d^* (deg)	$\alpha^{\rm Si\,II\lambda6355}$ $\beta^{\rm Si\,II\lambda6355}$	$\theta_d^{\rm Si\,II\lambda6355}$ (deg)	$\alpha^{\rm Ca\,II\,NIR3}$ $\beta^{\rm Ca\,II\,NIR3}$	$\theta_d^{\rm Ca\,II\,NIR3}$ (deg)
# 1	0.194 ± 0.125	0.209 ± 0.087	-0.061 ± 0.142 / $+0.478 \pm 0.131$	$23.8^{+7.9}_{-18.2}$ / $-33.5^{+4.8}_{-2.7}$	0.49 ± 0.13	$-31.4^{+6.6}_{-3.5}$	$+0.478 \pm 0.490$	$-32.0^{+26.1}_{-5.8}$
-14.5 d	0.077 ± 0.073		1.093 ± 0.895 / -2.347 ± 0.791		-1.95 ± 0.77		-2.045 ± 1.836	
# 2	0.008 ± 0.155	0.099 ± 0.080	-0.105 ± 0.005 / -0.108 ± 0.004	$2.1^{+1.3}_{-1.3}$ / $1.4^{+1.0}_{-1.0}$	-0.095 ± 0.012	$5.6^{+1.9}_{-2.0}$	-0.153 ± 0.015	$-6.2^{+2.4}_{-2.3}$
-11.4 d	-0.098 ± 0.078		0.0745 ± 0.046 / 0.050 ± 0.034		0.198 ± 0.071		-0.219 ± 0.086	
# 3	-0.037 ± 0.091	0.075 ± 0.080	-0.065 ± 0.005 / -0.058 ± 0.005	$2.4^{+1.6}_{-1.6}$ / $8.6^{+1.3}_{-1.4}$	-0.026 ± 0.018	$14.2^{+2.1}_{-2.2}$	-0.131 ± 0.018	$18.4^{+2.9}_{-3.4}$
-6.4 d	-0.065 ± 0.081		0.085 ± 0.055 / 0.310 ± 0.051		0.541 ± 0.097		0.748 ± 0.171	
# 4	0.109 ± 0.107	0.110 ± 0.100	$+0.0056 \pm 0.0044$ / -0.0026 ± 0.0036	$0.1^{+1.2}_{-1.2}$ / $4.3^{+1.0}_{-1.0}$	-0.013 ± 0.011	$5.3^{+1.8}_{-1.9}$	-0.107 ± 0.017	$20.9^{+2.7}_{-3.2}$
$+0.5$ d	-0.014 ± 0.099		0.021 ± 0.043 / 0.150 ± 0.037		0.186 ± 0.067		0.893 ± 0.184	
# 5	0.177 ± 0.119	0.186 ± 0.105	0.157 ± 0.014 / 0.103 ± 0.012	$-10.0^{+1.8}_{-1.7}$ / $-2.1^{+2.0}_{-1.9}$	-0.0098 ± 0.0195	$14.5^{+2.9}_{-3.3}$	-0.190 ± 0.037	$22.4^{+3.0}_{-3.7}$
$+14.5$ d	0.056 ± 0.102		-0.362 ± 0.071 / -0.073 ± 0.069		0.555 ± 0.143		0.991 ± 0.228	

Notes. *Dominant axes fitted excluding the Si II λ6355 and Ca II NIR3 features.
[a]Relative to the estimated peak on UT 2019-01-26.7/MJD 58509.7.

Downloaded from https://academic.oup.com/mnras/article/520/1/560/6988185 by University of Sheffield user on 26 May 2023

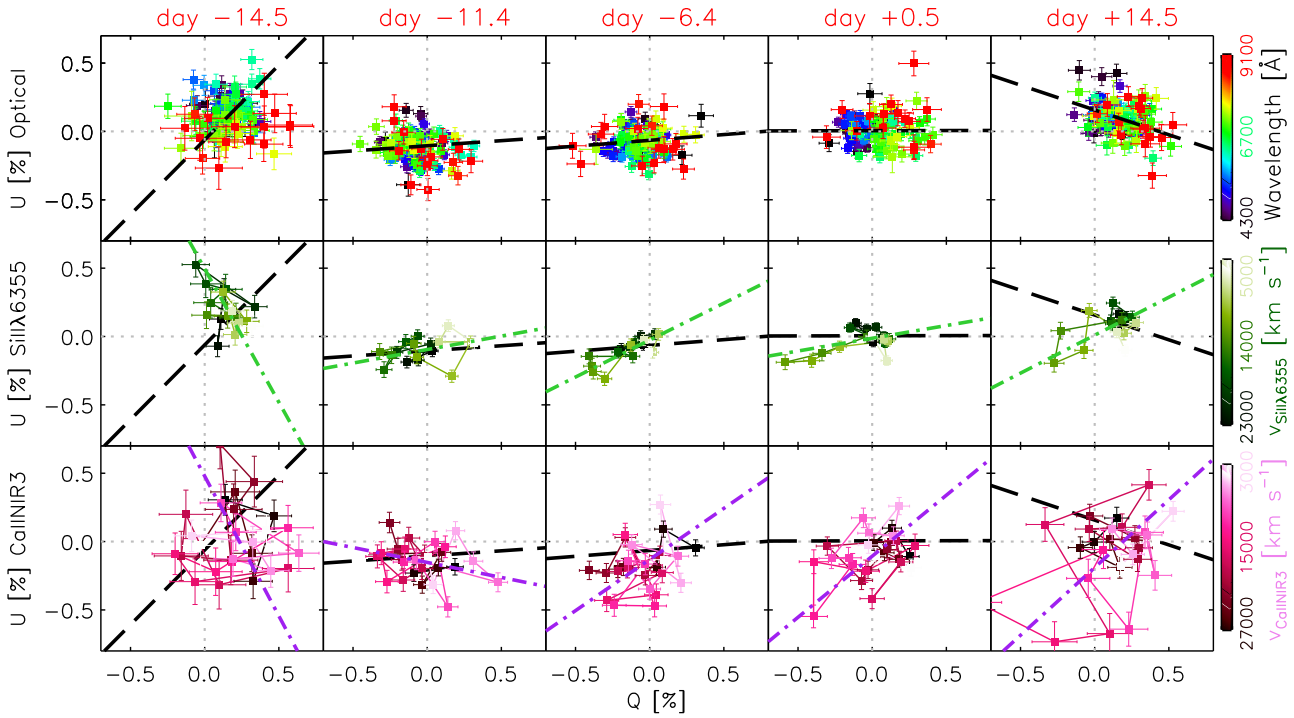

Figure 7. Intrinsic polarization of SN 2019np displayed on the Stokes Q–U plane. The top row shows the data over the wavelength range of 4250–9100 Å. The wavelength of each 30 Å bin is indicated by the colour bar on the right side. The middle and the bottom rows display the polarization for the Si II λ6355 and Ca II NIR3 features over the velocity ranges of 24 000–4000 km s^{-1} and 28 000–2000 km s^{-1}, respectively. The velocities are also indicated by the corresponding colour bars. The epochs of the observations are labelled with their phases at the top of each column. In each panel, the black long-dashed line shows the dominant axis calculated over the wavelength range 4250–9100 Å with the Si II λ6355 and Ca II NIR3 features excluded (the values of the fitted parameters α and β in equation (2) are listed in Table 2). In the middle and the bottom rows, the green and purple dot–dashed lines in each subpanel represent linear fits to the displayed data points that cover the Si II λ6355 and the Ca II NIR3 features, respectively.

3.5, 6.5, 11.5, 18.5, and 32.4 d, respectively. The first epoch is the earliest such measurement for any Type Ia SN to date.

3.3 The dominant axes in the Q–U plane

For each epoch of our ISP-corrected spectropolarimetry, we examine in the Stokes Q–U plane the axial symmetry of the ejecta of SN 2019np as they enter the extended photosphere. We do this separately for suitable wavelength ranges covering the continuum and the Si II λ6355 and Ca II NIR3 lines. This method was introduced by Wang et al. (2001); a different graphical rendering of the same data will be discussed in Section 3.4. Purely axially symmetric ejecta imprint a linear structure on the Q–U plane, since the orientation of the structure is defined by a single polarization position angle, while varying scattering and polarization efficiencies lead to deviations from a straight line. By projecting the data on to the best-fitting axis and measuring the scatter about this so-called dominant axis,

$$U = \alpha + \beta Q, \tag{2}$$

one may characterize the degree of axial symmetry of the SN ejecta (Wang et al. 2003; Maund et al. 2010a).

Fig. 7 displays the ISP-corrected Stokes parameters on the Q–U plane between days −14.5 and +14.5. The dominant axis of SN 2019np as determined from its polarization projected on the Q–U plane was derived by performing an error-weighted linear least-squares fit to the entire observed wavelength range ($4350 \leq \lambda \leq 9100$ Å) with the prominent and polarized Si II λ6355 and Ca II NIR3 features excluded. Data points covering the Si II λ6355 and Ca II NIR3 profiles were omitted in the top row, where the dominant axis appears as the black long-dashed line.

To examine the difference between the fits including and excluding the Si II λ6355 and Ca II NIR3 lines, we list the dominant axis and the corresponding position angles for both cases in Table 2. The dominant axes of SN 2019np fitted for both cases are consistent with each other within their 1σ uncertainties except for epochs 3 and 4, when SN 2019np reached its peak luminosity and the discrepancy between the two fits amounts to $\sim 2\sigma$. We consider the fits with both broad and polarized individual features excluded a more reasonable characterization of the orientation of the SN ejecta since these Si and Ca features generally exhibit significant deviations from the rest of the wavelength range (Leonard et al. 2005).

In the middle and bottom rows of Fig. 7, the directions of the symmetry axes of the Si II λ6355 and Ca II NIR3 features are shown by the green and purple dot–dashed lines, respectively. The fitting procedures were the same as for the continuum but over the velocity ranges from 24 000 to 0 km s^{-1} for Si II λ6355 and from 28 000 to 0 km s^{-1} for the Ca II NIR3 complex. The derived parameters are also listed in Table 2. On day −14.5, the spectropolarimetry over the optical range is poorly represented by a dominant axis. The Ca II NIR3 feature is barely described by the linear fits. Additionally, as shown by the Q–U diagrams for day −14.5, data points across Si II λ6355 deviate from the clustering in the continuum, indicating a conspicuous polarization across the line. However, owing to the relatively low signal-to-noise ratio (SNR) and the moderate level of polarization, it is hard to quantitatively determine whether Si II λ6355 and the ejecta of SN 2019np determined from the optical

Downloaded from https://academic.oup.com/mnras/article/520/1/560/6988185 by University of Sheffield user on 26 May 2023

continuum (as far as recorded by FORS2) follow different geometric configurations.

Starting from day −11.4, the ejecta of SN 2019np have developed a more discernible symmetry axis compared to day −14.5. This is indicated by the significantly reduced uncertainties in the linear least-squares fits to the polarimetry on the Q–U plane (see the α^*, β^*, and θ_d^* values in Table 2). The dominant axis of SN 2019np shows little temporal evolution between days −11.4 and +0.5 and rotates by ∼15° from days +0.5 to +14.5. Polar diagrams for Ca II NIR3 appeared very flocculent, and somewhat misaligned with the dominant axes of Si II λ6355 and $p^{\rm cont}$. Qualitatively, the temporal evolution of Si II λ6355 and Ca II NIR3 features are similar. This can be seen from the middle and bottom rows of Fig. 7. Not considering the first epoch, the dominant axis of Si II λ6355 was roughly constant and stayed close to that of the continuum until both rotated in opposite directions on day +14.5. Not considering day −14.5, we suggest that SN 2019np belongs to the spectropolarimetric type D1 (Wang & Wheeler 2008), in which a dominant axis can be determined while the scatter of the data points about the dominant axis is conspicuous. At the earliest epoch, a dominant axis cannot be clearly identified, and the continuum polarization measurements cluster around a location offset from the origin.

Apart from Si II λ6355 and Ca II NIR3, there are numerous minor peaks scattered all over the polarization spectra. Nominally, these features are significant at ∼2σ and occasionally at 3σ. Careful quality control of the data and our reduction procedures have not identified them as artifacts, although some of them will undoubtedly be spurious. Most of them are volatile and, in consecutive observations, do not appear at the same location. This can be expected because the spectral features form in layers with different abundances (see Section 4.3). In our analysis in Section 4, we will refer to them as 'wiggles'.

3.4 Line polarization in polar coordinates

To further visualize the geometric distribution of the Si II and Ca II opacities in the ejecta of SN 2019np, we cast the line polarization into the format of polar plots where the radial axis indicates the velocity across the spectral profile and the angle from the reference direction represents the polarization position angles on the plane of the sky at the corresponding wavelength [introduced by Maund et al. (2009), and see e.g. Reilly et al. 2016; Hoeflich 2017; Stevance et al. 2019]. Fig. 8 presents the polar plots for the Si II λ6355 and Ca II NIR3 lines from days −14.5 to +14.5.

On day −14.5, relatively highly polarized Si II is present mostly above the photospheric velocity. The orientation of the Si-rich material appears to be different from the direction of the dominant axis as determined in Section 3.3 and indicated by the grey sector in the left-hand panel of Fig. 8. Note that the angular size of the fan-shaped sector represents the 1σ uncertainty of the position angle. Unlike the Si-rich material that is confined in a relatively narrow range in position angle, the Ca-rich component exhibits a more diverse radial profile. The Ca-rich material below the high-velocity (hv) component at ∼20 000 km s^{-1} shows a range in position angle that is consistent with (i) the dominant axes plotted as black dashed lines in the left-hand panels of Fig. 7, and (ii) the grey fan-shaped sector in the left-hand panel of Fig. 8. However, the component above the high-velocity threshold exhibits a range in position angle that is distinct from the dominant axis but has a similar orientation as the Si-rich material above the photosphere. Therefore, the high-velocity Si-rich and Ca-rich components seen on day −14.5 are likely to share a similar geometric distribution that differs from that of the optical continuum.

On day −11.4, the dominant axis has rotated relative to day −14.5, as indicated by the position angle of the grey fan-shaped sector in the second polar plot of Fig. 8. Additionally, based on its reduced angular extent, we deduce that the symmetry axis of the SN ejecta becomes more prominent and well-defined as the photosphere progressively recedes. Most of the Si- and the Ca-rich material gets almost aligned with the optical dominant axis, with larger offsets seen in the radial profile of the Ca-rich component. This alignment suggests that a similar axial symmetry is shared by the total ejecta and the line opacities. An overall similar geometry of SN 2019np can be derived from the polar plots for days −6.4 and +0.5 (third and fourth panels in Fig. 8), which indicate no significant evolution since day −11.4. From day −11.4 to +0.5, the orientation of the dominant axis persists. The widths in velocity of the fan-shaped sectors display an overall decreasing trend for both the Si-rich and the Ca-rich components. Since the line velocities decrease and the high-velocity components diminish with time, the polarization signal measured at the high-velocity end decreases and becomes less significant as indicated by the large uncertainties.

By day +14.5, the dominant axis has rotated compared to that measured during the rising phase of SN 2019np. The scatter has increased again in radial profiles of the Ca-rich material, suggesting a more complex structure of the line-forming regions in the more inner layers of the SN ejecta. The high-velocity component has become indiscernible in the flux spectrum (Figs 5 and 6, and Sai et al. 2022).

An overall property of the polar diagrams is their patchy appearance, especially in Ca II NIR3 (Fig. 8). These 'flocculent' structures tend to become gradually less conspicuous with time, and increase again at day +14.5. The time evolution of the continuum polarization is shown in Fig. 9.

4 NUMERICAL MODELLING

This section conducts a quantitative study of the degree of asphericity of SN 2019np inferred from the observations described in Section 3. We also investigate their temporal evolution and interpret the nature of the polarization variations on small wavelength scales. As a baseline, we will use an off-centre delayed-detonation model (Khokhlov 1991), namely the explosion of an $M_{\rm Ch}$ WD in which a deflagration front starts in the centre and transitions to a detonation for reasons described in Section 4.1.

A low level of polarization along the continuum spectrum of a SN is most likely generated by spherically symmetric ejecta leading to complete cancellation of the electric vectors. However, an aspherical but rotationally symmetric object may also be viewed along its symmetry axis, which has the same effect. To distinguish these two possibilities, we will use both the polarization over the quasi-continuum and the modulation of the polarization across major spectral features in order to separate the intrinsic asphericity and the polarization actually observed from a certain direction. In our analysis, we will employ an approach of minimum complexity rather than fine tuning the parametrized geometry to optimize the fitting. The modelling will address whether the 0.1–0.2 per cent polarization variations with wavelength in the quasi-continuum seen at all epochs can be understood in terms of opacity variations. Furthermore, we will discuss whether the temporal and spectral resolution of our VLT spectropolarimetry is sufficient to detect and probe any small-scale structures in density and/or abundances.

The VLT spectropolarimetry of SN 2019np between days −14.5 and +14.5 was analysed through simulations employing modules of

Downloaded from https://academic.oup.com/mnras/article/520/1/560/6988185 by University of Sheffield user on 26 May 2023

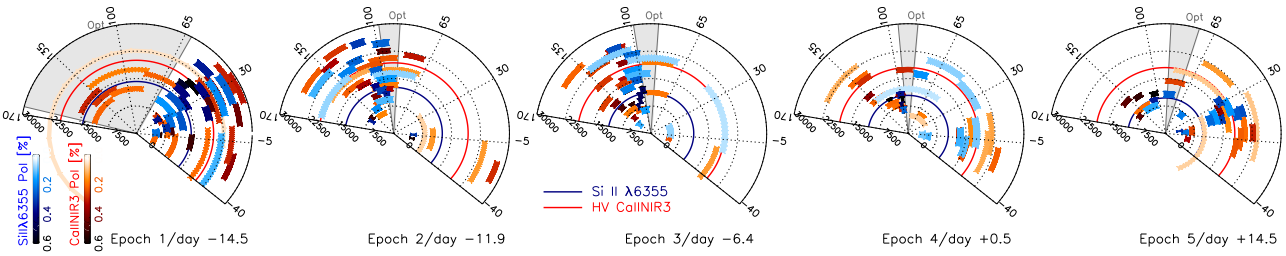

Figure 8. Polar plots of the polarization of SN 2019np across the Si II λ6355 and Ca II NIR3 lines at all five epochs. In each panel, the radial distance and the angle represent the expansion velocity and the polarization position angle, respectively. The centre of each fan-shaped bin gives the average position angle calculated over the velocity range covered by the radial extent of the bin. The angular widths of the fan-shaped bins represent the 1σ uncertainty on the position angle, rather than the underlying physical dimensions. The velocity is labelled in km s^{-1}, and the celestial position angles are measured in degrees from north to east. The blue and the orange colour bars indicate the ISP-corrected polarization degree across the Si II λ6355 and Ca II NIR3 profiles, respectively. The data have been rebinned to 30 Å for better visualization. The direction of the dominant axis is shown by grey-shaded regions with their angular width representing the 1σ uncertainty (i.e. θ_d^* in Table 2). The blue and red semicircles mark the estimated photospheric velocity and the high-velocity component as measured from the absorption minima of the Si II λ6355 and Ca II NIR3 lines, respectively.

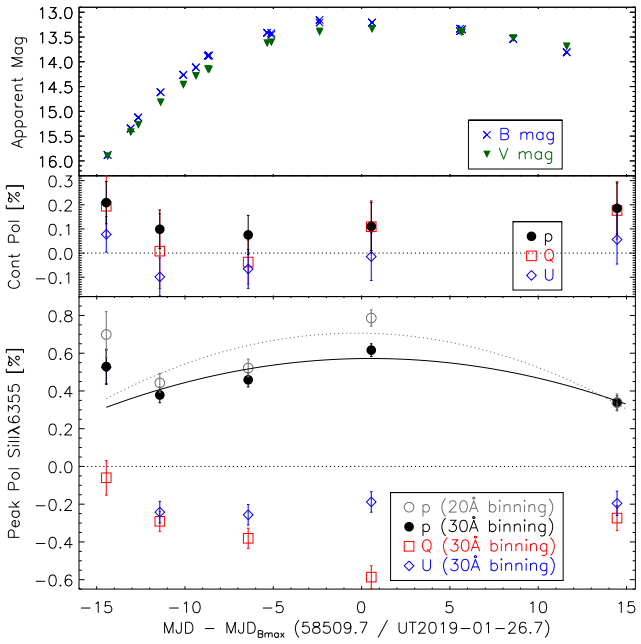

Figure 9. Temporal evolution of the intrinsic polarization of SN 2019np from days −14.5 to +14.5. The *B* and *V* light curves (from Burke et al. 2022) are displayed in the top panel. The middle panel gives the continuum polarization calculated from the error-weighted mean values of the Stokes parameters in the range of 6400–7000 Å. The bottom panel presents the peak polarization measured across the Si II λ6355 line. Values measured with both 30 Å and 20 Å bin sizes are plotted as labelled. Second-order polynomial fits to either bin size are indicated by the solid black and dotted grey curves, respectively.

the HYDrodynamical RAdiation (HYDRA) code[5] (Höflich 1995a, 2003; Penney & Hoeflich 2014; Hoeflich et al. 2021; Hristov, Hoeflich & Collins 2021). HYDRA solves the time-dependent radiation transport equation (RTE) including the rate equations that calculate the nuclear reactions based on a network with 211 isotopes and statistical equations for the atomic level populations, the equation of state, the matter opacities, and the hydrodynamic evolution. The resulting polarization is obtained by post-processing the given level populations and the density and abundance structure through a Monte Carlo (MC) approach (Khokhlov 1991; Höflich 1995a, 2003; Penney & Hoeflich 2014; Hoeflich et al. 2021; Hristov et al. 2021). Atomic models were considered for the ionization stages I–III of C, N, O, Ne, Mg, Na, Ca, Si, S, Ar, V, Ti, Cr, Fe, Co, and Ni, but without forbidden transitions. For the luminosity evolution of the multidimensional model as a function of time, a spherical reference model with 911 depth points was adopted, which is adequate considering the small deviation from spherical symmetry. Moreover, the timescales are dominated by the inner layers which are almost spherical in off-centre delayed-detonations, whereas the spectra are formed in the photosphere. This allows us to compare the observations with snapshots of the multidimensional model, neglecting time derivatives in the rate and radiation transport equations.

For the polarization spectra, we use ∼700 frequency counters between 2800 and 10 200 Å. The resulting spatial discretization corresponds to a formal spectral resolving power of $R \approx 500$, which matches that of the observations ($R \approx 440$, Section 2). However, in a rapidly expanding atmosphere with gradients, the spatial resolution degrades R to ∼150 since the solution of the radiation transport equation depends on the spatial gradients of the physical quantities. Simulating a large number of configurations by multidimensional models is prohibitively expensive. Therefore, we employ a scattering approach with a thermalization depth to find and discuss estimates for the degree of asphericity in the surface as well as deeper layers (Höflich 1991).

The continuum polarization may be caused by an aspherical electron-scattering photosphere or an off-centre energy input or both (Höflich 1995c; Kasen 2006; Bulla et al. 2016a) (see Fig. 10). In the spectra of a Type Ia SN, opacities from bound-bound transitions form a wavelength-dependent quasi-continuum and also produce individual spectral features. The quasi-continuum may exhibit polarization signals when the sizes of any opacity clumps are comparable to the free mean path of Thomson scattering. One should keep in mind that, in the high Thomson optical-depth regime ($\tau \gtrsim 3$–4), the continuum polarization in the quasi-continuum will be lower compared to that at $\tau \approx 1$ and reach an asymptotic limit for large optical depths since any information about asphericity will be blurred by multiple scattering (see e.g. figs 1 and 5 of Höflich 1991). If the opacity of the quasi-continuum becomes much larger than the optical depth of

[5]Many of the HYDRA modules are regularly used by other groups and are available on request to PH.

Downloaded from https://academic.oup.com/mnras/article/520/1/560/6988185 by University of Sheffield user on 26 May 2023

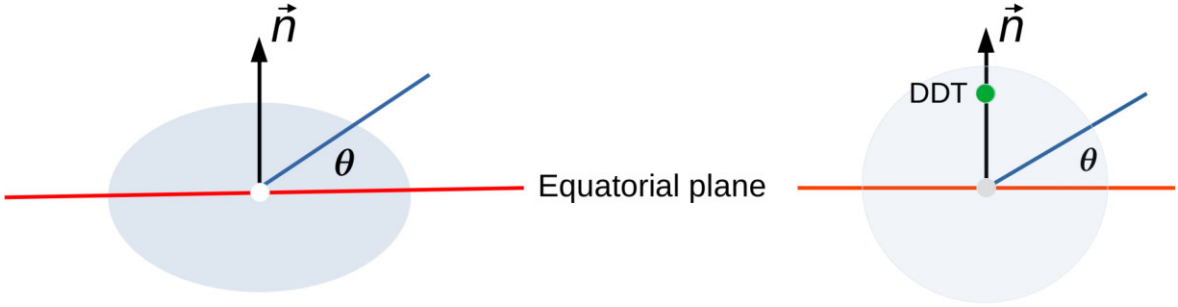

Figure 10. The symmetry axis $\vec{n}$ (black arrow) is defined by the minor axis of a rotationally symmetric ellipsoid (i.e. an oblate spheroid, left plot) or by the vector (right plot) through the centre (grey dot) and the location of the DDT (green dot). The equatorial plane E (red) is given by $\vec{n}\,\vec{x} = 0$ with $\vec{x}$ spanning E. The viewing angle θ is the angle between the plane E and the direction to the observer (blue line). $\theta = +90°$, $-90°$, and $0°$ correspond to the north pole, south pole, and the equator, respectively. As common, θ is measured counterclockwise.

the Thomson scattering, the degree of polarization $p \propto \tau_{sc}$, where τ_{sc} denotes the electron-scattering optical depth of layers at which photons thermalize.

4.1 The reference model

As the spherically symmetric reference, we adopt the delayed-detonation Model 25 for a normal-bright Type Ia SN from Hoeflich (2017) because it shows light-curve properties very similar to those of SN 2019np. The explosion disrupts a WD with mass close to M_{Ch}. Burning starts as a deflagration front near the centre and transitions to a detonation by the mixing of unburned fuel and hot ashes (Khokhlov 1991).

The explosion originates from a C/O WD with a main-sequence mass of 5 $M_\odot$ as the progenitor star, solar metallicity, and a central density $\rho_c = 2 \times 10^9$ g cm^{-3}. The deflagration–detonation transition was triggered when the density at the front had dropped below 2.5×10^7 g cm^{-3} when $\sim$0.24 $M_\odot$ of the material had been burned by the deflagration front. For the construction of the off-centre delayed detonation transition (DDT), we follow the description of Livne (1999) that has been previously employed (Höflich et al. 2006b; Fesen, Höflich & Hamilton 2015; Hoeflich et al. 2021). To terminate the deflagration phase, the delayed-detonation transition is triggered with the mass-coordinate M_{DDT} as an additional free parameter. The time series of the flux and the polarization spectra were generated without further tuning of the model parameters. The photometric properties predicted by the spherical model are similar to those measured for SN 2019np, namely $\Delta m_{15}(V/B) = 1.14/0.68$ mag (Model 25) and 1.04/0.67 mag (Sai et al. 2022).

According to the above prescription, the axial symmetry of the SN model is defined by the location(s) of the point(s) where the deflagration-to-detonation transition took place. The asphericity in the density distribution near the surface layers was characterized by introducing an additional free parameter when modelling the continuum polarization at the earliest phase. For the actual implementation see the last paragraph of this subsection. The symmetry axis that determines the geometric properties of the outermost layers and that which is defined by the location of the deflagration-to-detonation transition in the inner regions are not correlated with each other, since the latter is stochastic and expected to take place deeper in the WD. As the DDT is turbulently driven in the regime of distributed burning, its location depends on the ignition process of the thermonuclear runaway, namely multispot or off-centre ignition, and initial magnetic fields. In contrast to the inner symmetry axis, that of the surface layers is likely determined by the direction of the angular momentum of the progenitor system, i.e. the equatorial plane of a companion or the plane of an accretion disc. Since the luminosity originates from the energy source that is well below the photosphere in the first few days after the SN explosion, and the outermost layers do not affect the emission at later phases, our simulations treat these two symmetry axes as independent parameters.

In Fig. 11, we present the mass above the photosphere as a function of time (left-hand panel) and the radial distribution of the chemical abundances as a function of expansion velocity (middle panel). Overall, the exploding envelope has the familiar onion-shell-like structure. However, the onion is no longer spherical but elongated as a result of the off-centre DDT (see also fig. 2 in Hoeflich et al. 2021). In the left-hand panel, we also mark the times of the VLT spectropolarimetry with respect to both the estimated time of the explosion and the *B*-band light-curve peak. The earliest spectropolarimetry to date of any Type Ia SN on day -14.5 probes the outermost $\lesssim (2.5–3) \times 10^{-3}$ M_{WD} layer of the exploding WD, corresponding to a mass of $\lesssim 4 \times 10^{-3}$ $M_\odot$. As deduced from the red triple-dot-dashed curve, at such an early phase, the exponential index of the radial density distribution is $n \approx 13–14$. In the middle panel of Fig. 11, we mark the locations of the photosphere at each epoch of the VLT spectropolarimetry in velocity space. Note that the absorption minimum of, for example, Si II λ6355 does not measure the expansion velocity at the photosphere but the average projected velocity towards an observer. The difference compared to the expansion velocity at the photosphere is particularly large in zones with steep density profiles. Since the photosphere recedes over time, multiepoch spectropolarimetry can tomographically map out the degree of asphericity at different chemical layers. As indicated by the middle panel of Fig. 11, the cadence of the VLT observations of SN 2019np only provides a resolution in expansion velocity of $\sim$6000 km s^{-1}, at which a discrimination of any structures smaller than several thousand km s^{-1} in the radial direction is not possible. For a detailed discussion, see Section 6.1.

We employ a delayed-detonation model considering the fact that C II was seen in the first epoch on day -14.5 (Fig. 1), corresponding to the very outer layers of $\lesssim 4 \times 10^{-3}$ $M_\odot$, making a sub-M_{Ch} explosion an unlikely candidate even for the case of C/He mixtures (Shen & Moore 2014). Note that M_{Ch} explosions may have a thin H/He-rich surface layer as a result of the accretion phase but at a significantly smaller mass, $(1–5) \times 10^{-4}$ $M_\odot$ (Hoeflich et al. 2019), an amount below our numerical resolution. Therefore, we neglect the H/He layer in our simulation.

Downloaded from https://academic.oup.com/mnras/article/520/1/560/6988185 by University of Sheffield user on 26 May 2023

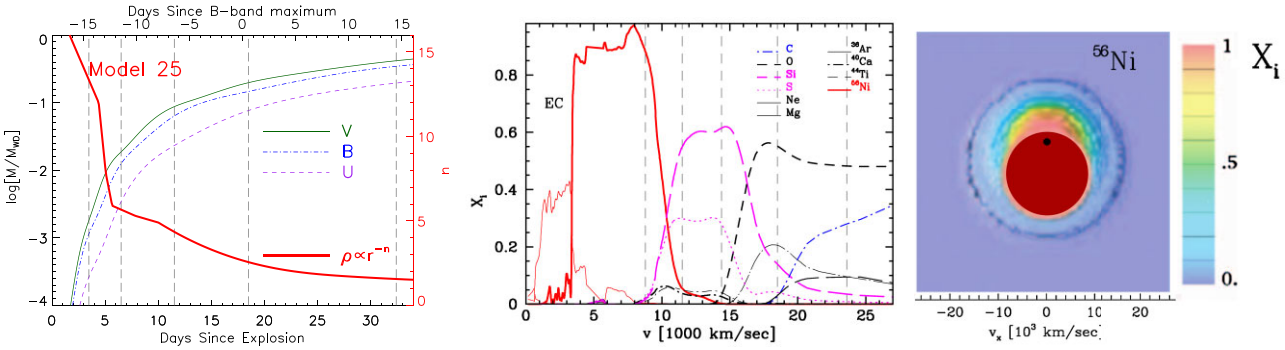

Figure 11. *Left:* The mass above the photosphere as seen by photons in the *U*, *B*, and *V* bands as a function of time for the normal Type Ia SN calculated in the off-centre angle-averaged version of the delayed-detonation Model 25 (Hoeflich 2017). The exponential index (n) of the radial density distribution at the position of the photosphere as a function of time is also shown by the red triple-dot–dashed line. The five epochs of VLT spectropolarimetry are marked by grey vertical dashed lines. *Middle:* Angle-averaged abundance structure as a function of expansion velocity, also calculated using Model 25. Vertical grey-dashed lines indicate the location of the scattering photosphere – that is, $\tau_{sc} = 1$ at the times when the VLT spectropolarimetry was obtained. The region with electron-capture elements is indicated by EC. *Right:* The ^{56}Ni distribution as seen above the photosphere on day +14.5 based on the hydrodynamical simulation of the off-centre detonation. The mass fraction of off-centre ^{56}Ni above the photospheric radius (dark-red) is ∼6 per cent. At this phase, the radius of the photosphere is close to the location (black dot) where the deflagration-to-detonation transition takes place, and it expands with ∼7000 km s^{-1}. The mass fraction is colour-coded in a domain size of ±23 500 km s^{-1}.

In Model 25, the early-time spectra originate from the region with incomplete explosive carbon burning and an inward-increasing contribution by explosive oxygen burning (Fig. 11). By the time of maximum light, the photosphere is formed in layers of complete oxygen burning and partial silicon burning as indicated by the presence of Ar and Ca. The emergence of Ar lines in the mid-infrared was predicted by our models. In SN 2014J, they were detected by Telesco et al. (2015). At ∼2 weeks after peak luminosity, the spectrum on day +14.5 obtained by our last epoch of VLT observations is formed at the interface between partial, distributed silicon burning and with burning to nuclear statistical equilibrium (NSE). The position of this layer coincides with the location where the DDT has been triggered. Note that in our simulation the point of the DDT does not lead to a strong refraction wave (Gamezo, Khokhlov & Oran 2005) as in all spherical delayed-detonation models (Khokhlov 1991). The innermost layers undergo weak reactions under NSE conditions, resulting in the production of electron-capture (EC) elements.

An asphericity in the outermost layers as indicated by the positive detection of the continuum polarization at the first epoch (see Section 3.2) is not produced by our hydrodynamical reference model. To estimate the degree of asphericity at that early epoch, we describe the density structure of SN 2019np by stretching along the radial direction using an oblate ellipsoid with the axis ratio as a free parameter. The density and abundance structure are directly taken from our reference model, transforming the distance from the centre of an element as $r(m) \Rightarrow r(m, \theta)$ (Höflich 1991). In the toy models for the continuum developed in Section 4.2, we treat the orientation as a free parameter. For reasons of computational feasibility of the full model, we assume that the symmetry axes of the density and abundances are aligned. When the deflagration front has burned ∼0.25 M$_\odot$, we trigger the detonation by mixing burned and unburned fuel at $M_{DDT} = 0.5$ M$_\odot$,[6] the so-called Zel'dovich reactivity gradient mechanism (Zel'Dovich et al. 1970).

[6]Using the amplitude of the Si II λ6355 polarization as the criterion, we chose this mass fraction from a set of intermediate models for levels of 0.1, 0.3, 0.5, and 0.9 M$_\odot$. For the Monte Carlo post-processing to obtain p presented in this paper, a number of particles per resolution element has been used to obtain a statistical absolute error of $\lesssim$ 0.015 per cent.

4.2 Continuum polarization

On days −14.5 (the first epoch) and +14.5 (the fifth and last epoch), the level of the continuum polarization has been measured as 0.21 ± 0.09 per cent and 0.19 ± 0.10 per cent, respectively, both at a ∼2σ level (see footnote in Section 3.2). The former corresponds to the very outer layers and the latter probes the inner layers near the position where the deflagration-to-detonation transition takes place. Between day −11.4 (second epoch) and day +0.5 (fourth epoch), the continuum polarization was consistent with zero within the uncertainties (see Section 3.2).

At early times, the thermalization depth of the photons emitted by an SN is large (i.e. $\tau \gtrsim 3$), and the polarization degree reaches its asymptotic value [see figs 1 and 11 of Hoeflich, Mueller & Khokhlov (1993) and Höflich (1995c), respectively, and the inset in Fig. 12]. The maximum polarization degree is expected when $\tau \approx 1$ (Höflich 1991). Linear polarization produced by aspherical density structures follows the relation $p \propto \sin^2\theta$, where θ is the angle between the polar direction and the observer. As the radial density exponent n is high at the first epoch ($n \approx$ 13–14; see the left-hand panel of Fig. 11), a minimum axis ratio of 1.25–1.4 can be inferred from the continuum polarization of 0.21 ± 0.09 per cent on day −14.5 (see the left-hand panel of Fig. 12). For an equator-on perspective ($\theta = 0°$), the high axis ratio implies asphericity in excess of 30 per cent in the 4 × 10^{-3} M$_\odot$ of the carbon-rich layers in the outermost part of the exploding WD (see Fig. 11).

Only three days later, on day −11.4, the continuum polarization had dropped rapidly to a level consistent with zero. By contrast, for a constant global asphericity, the degree of polarization would increase with time because (i) the density slope becomes flatter (see the left-hand panel of Fig. 11), and (ii) the thermalization optical depth decreases to ∼1 as the SN reaches maximum light, when the quasi-continuum opacity in the iron-rich region becomes comparable to, or larger than, the Thomson opacity (see e.g. fig. 2 in Höflich, Mueller & Khokhlov 1993).

Therefore, the rapid decrease in continuum polarization observed in SN 2019np suggests that the large-scale asphericity in the density structures seen at the earliest phase is limited to the very outer layers. We find that an additional structural component is only required at the first epoch. For all deeper layers, we do not have to impose any

Downloaded from https://academic.oup.com/mnras/article/520/1/560/6988185 by University of Sheffield user on 26 May 2023

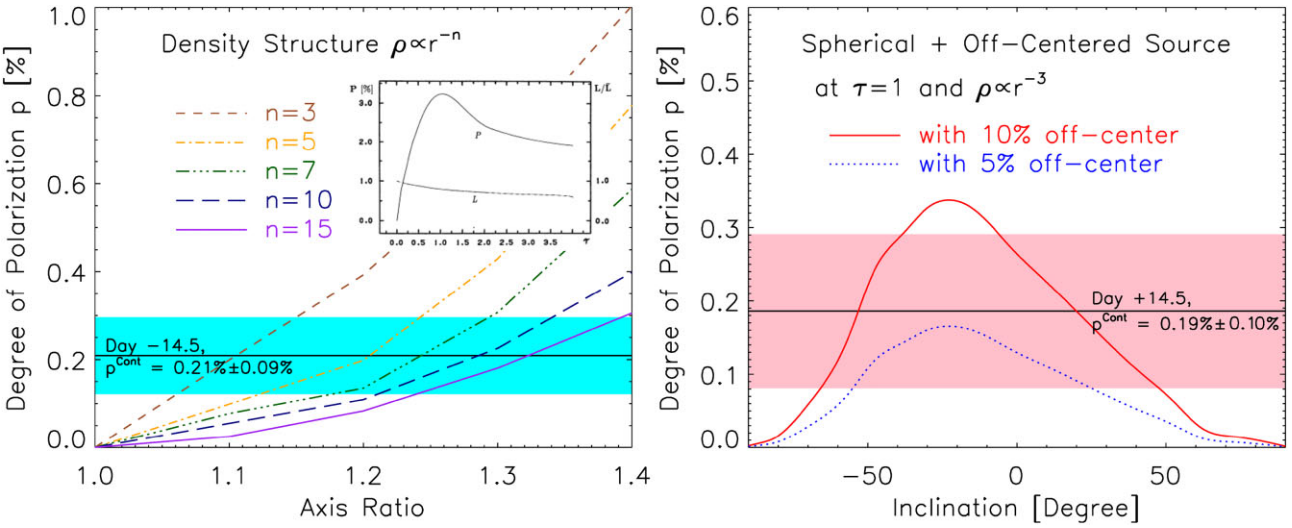

Figure 12. *Left:* Continuum polarization as a function of asphericity for an oblate ellipsoidal scattering-dominated photosphere viewed equator-on. A steep density gradient can be expected at early phases (see Fig. 11), when the polarization approaches the limit of large optical depth. The exponential index of the radial density distribution on day −14.5 can be best represented by configurations with $n \approx 13$–14 (the left plot of Fig. 11). The horizontal line and the cyan-shaded area indicate the level and the associated uncertainty of the continuum polarization (respectively) measured on day −14.5. Therefore, an axis ratio between ∼1.25 and 1.4 is expected. To aid the discussion in the text, the inset panel shows the continuum polarization as a function of thermalization optical depth for an oblate ellipsoid with an axis ratio of 2 and $\rho \propto r^{-2}$ (from Höflich 1991). *Right:* The degree of continuum polarization produced by a spherical photosphere plus an off-centre energy source as a function of viewing angle. For the illustration of the effect of an off-centre energy source, a radial density distribution index $n = 3$ and an optical depth $\tau = 1$ are chosen to represent the SN photosphere around two weeks after maximum brightness (see Fig. 11). The horizontal line and the pink-shaded area mark the level and the error of the continuum polarization, respectively, on day +14.5.

asphericity on the density distribution. The difference in polarization position angle between the surface and the deeper layers may be attributed to the additional structural component.

On day +14.5, the continuum polarization of SN 2019np exhibited an increase to 0.19 per cent ± 0.10 per cent, although the scattering optical depth had decreased significantly well below $\tau_{sc} = 1$, where $p \propto \tau_{sc}$, and, hence, a decrease in p may be expected. As will be discussed in Section 4.3, the continuum polarization can be understood as a consequence of our off-centre DDT Model 25, which produces an aspherical distribution of ^{56}Ni, and thus an inhomogeneous central energy source.

An off-centre energy source is needed because the quasi-continuum dominates the Thomson scattering causing thermalization at low τ_{sc} and, thus, only photons with grazing incidence on the outer photosphere get polarized. The reason is that photons scattered into the direction of their travel, the Poynting vector, are unpolarized whereas light scattered orthogonally to the Poynting vector is 100 per cent polarized. Radially traveling photons are most likely to escape when they are scattered along the Poynting vector, whereas grazing-incidence photons can escape most easily when they are radially scattered by 90°.

A similar increase of the continuum polarization after maximum light was reported for SN 2019ein, namely 0.28 ± 0.10 per cent on day +10 and 1.31 ± 0.32 per cent on day +21 (Maund et al. 2021; Patra et al. 2022). This rise of the broad-band polarization at late phases was also attributed to the emergence of an aspherical central energy input as the photosphere reaches the Si/Fe interface (Patra et al. 2022).

As a first step, we quantify the level of the asphericity in the ^{56}Ni distribution required for a toy model that does not depend on details of the explosion process. We estimate the amount of off-centre ^{56}Ni at the photosphere relative to the main, symmetric component of the ^{56}Ni distribution based on previous simulations (Höflich 1995b). Motivated by the low continuum polarization between days −11.4 and +0.5 (see Section 3.2), we assume[7] that the low continuum polarization by any global asphericity in the density at the photosphere can be neglected and, based on Model 25, that the off-centre source is at about the photosphere (see the right-hand panel of Fig. 11). For the toy model, a point-like off-centre source at $\tau_{sc} = 1$ in a spherical envelope is assumed to obtain a first-order estimate.

The relative contribution by the off-centre component at day +14.5 to the total energy input at the photospheric level is found to be between 5 and 10 per cent (see the right-hand panel of Fig. 12). Using as reference the axis defined by the centre and the location the DDT, a tangential energy source causes a flip in the polarization angle or, in the Q–U diagram, the polarization axis should rotate by 90°(Höflich 1995c). However, only ∼70° are observed relative to the layers seen at day −14.5. Thus, our toy model predicts a difference between the symmetry axes of the outer structural component and the inner layers which causes a change in PA in the Q–U diagram of about 20° compared to day +0.5 (Fig. 7). This estimate is obtained by the vectorial addition of the polarization contributions by the off-centre source and the spherical source.

Although a change in position angle from day −14.5 to −11.5 to +14.5 is hard to measure in SN 2019np owing to the very low intrinsic continuum polarization, we suggest that the rotation of the dominant axis fitted to the same optical wavelength range as above (see Fig. 7) is compatible with the prediction of an off-centre energy source beginning to be exposed to the observer at this phase.

[7]As shown in Section 4.3, we cannot allow a large-scale density asymmetry in Model 25.

Downloaded from https://academic.oup.com/mnras/article/520/1/560/6988185 by University of Sheffield user on 26 May 2023

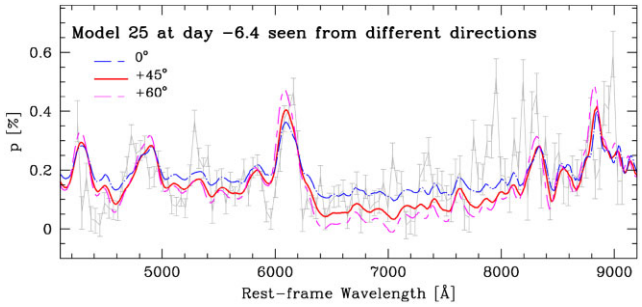

Figure 13. Estimating the viewing angle θ from polarization spectra (see the text). As examples, the full polarization spectrum of the off-centre DDT Model 25 at day −6.4 is shown for inclinations θ of about 0° (blue, equator-on), 45° (red), and 60° (cyan), and, as reference, the intrinsic polarization of SN 2019np at a corresponding resolution (grey). The estimate of θ is based on all epochs, and the error in θ is constrained by the uncertainty of the observations. For $\pm 90^{o}$, the polarization is close to zero. Note the sensitivity of the ratio between line and continuum polarization to θ.

One of the major effects of the very steep density slope in the outer layers is that even the small ∼0.2 per cent continuum polarization ∼3.5 d after the SN explosion implies a significant aspherical density distribution. The polarization of SN 2019np at the earliest epoch is higher than that measured in other Type Ia SNe at later phases, which are closer to epoch 2 on day −11.4 and epoch 3 on day −6.4 of SN 2019np. For example, 0.10 ± 0.07 per cent was observed in SN 2019ein (Patra et al. 2022) on day −10.9, and 0.06 per cent±0.12 per cent in SN 2012fr (Maund et al. 2013) on day −11.

However, the 0.21 ± 0.09 per cent continuum polarization of SN 2019np on day −14.5 (∼3.5 d after the explosion) is comparable to the marginal detection of a 0.20 per cent ± 0.13 per cent continuum polarization in SN 2018gv on day −13.5, ∼5 d after the explosion (Yang et al. 2020). At that moment, the density exponent in SN 2018gv had dropped to ∼9–10 (see the left-hand panel of Fig. 12 and fig. 21 of Yang et al. 2020). This leads to a ∼10–35 per cent deviation from spherical symmetry within the outermost ∼(0.5–2) × 10^{-2} M_{WD} for an equator-on configuration. The cases of SNe 2019np and 2018gv may provide a hint that any asphericity in the outer layers of normal-bright Type Ia SNe becomes apparent in polarization only during the very earliest phases and thereafter quickly almost vanishes. Therefore, given the high-density gradient near the surface layers of the ejecta of Type Ia SNe, a low but non-zero continuum polarization measured in the first few days after the explosion does not necessarily imply a low deviation from sphericity in their outermost layers.

4.3 Polarization spectra

The spectral evolution of SN 2019np is similar to that of other normal-bright Type Ia SNe (Sai et al. 2022), enabling us to compare the polarization spectra of SN 2019np with the models for normal Type Ia SNe discussed by Höflich (1995a). The inclination was obtained by comparing the direction-dependent synthetic polarization spectra to those of SN 2019np at all epochs and minimising the χ^2 averaged over 100 Å-wide bins. To fit the evolution of the polarization spectra (see Section 3.4 and Figs 6 and 9), we find that a viewing angle of $\theta = +45^{\circ} \pm 10^{\circ}$ is the most plausible approximation of the actual case (Fig. 13).[8] In Fig. 16, the off-centre delayed-detonation model viewed at this angle is in good overall agreement with the observations of SN 2019np.

In Model 25, the polarization across Si II λ6355 is formed within an extended geometrical structure between 9000 and 27 000 km s^{-1} that undergoes complete and incomplete oxygen burning in velocity (the middle panel of Fig. 11, where the velocity of the photosphere at the time of the observations is indicated). In the outermost region of partial explosive oxygen and carbon burning, the polarization of Si II λ6355 is weaker since its abundance diminishes with increasing velocity. At early times, this line forms close to the region with $\tau_{sc} = 1$. Because the polarization by electron scattering is mostly formed in the range $0.1 < \tau_{sc} < 1$, the polarization across Si II lines is generally low. The Si polarization increases as the photosphere continuously recedes and, without the structural component, reaches its peak when the photosphere enters the layers with quasi-equilibrium conditions around the Si group. Thus, the polarization in Si II λ6355 increases with growing distance between the optical depth at a given wavelength and the layer with $\tau_{sc} \approx 1$, which is always more internal. Any aspherical distribution is expected to be most prominent around this phase, when the photosphere passes the inner boundary of the explosive C- and O-burning, and the QSE(Si)/NSE interface becomes exposed (Höflich et al. 2006a). After peak luminosity, the polarization of Si II λ6355 decreases because the quasi-continuum opacities increasingly dominate the electron scattering.

Apart from Si II λ6355, the polarization over a quasi-continuum wavelength range also increases in the same region that forms various other spectral features, which are resolved (see Figs 14, 15, and 16). This concerns the entire wavelength range occupied by blends of the Fe group, Si II, S II, and O I. Depending on time, features in the polarization spectra appear around (for example) 4400, 4800, 5400, 5800, 6800, 7200, 7500, 8300, and 9000 Å (Fig. 16). Overall, thousands of overlapping lines are involved (see e.g. figs 1 and 2 of Hoeflich et al. 1993). The variations in this quasi-continuum depend on the velocity gradients, the abundances, and the ionization level. The polarization is very sensitive to this pattern as it influences the thermalization optical depth by individual components because spectral lines mostly depolarize. In flux spectra, these variations are mostly blurred because photons are absorbed and emitted, but they are visible in the line-formation radii traced by spectropolarimetry (Fig. 15). As a result, spectropolarimetry is effectively much more sensitive to spectral lines than flux spectroscopy because its observable signatures are much less volatile. Nevertheless, some individual patterns can be identified by comparing the line identifications (Figs 1–5 and 15) and, from the models, by variations in the wavelength-dependent radii of line formation as presented in Fig. 14. For instance, the rather persistent feature at 9000 Å can be attributed to a strong Fe II + Co II blend that becomes obvious as a change in the thermalization radius and appears in both observed and synthetic spectra (Fig. 16).

In the models, a maximum or minimum in polarization is produced if the thermalization optical depth is above or below $\tau_{sc} \approx 1$, respectively. Owing to the sensitivity of the polarization, maxima in the observations can be minima in the synthetic spectra for moderately strong blends which appear in the optical depth (Fig. 14). One example is the Fe/Co blend at ∼9000 Å. This feature toggles with time between maxima and minima in both theory and observations. At most epochs, the changes in model and observations are synchronized, except for days −11.4 and +0.5. Another example is the S/Fe

[8]For example, at maximum light, compared to $\theta = +45^{\circ}$, the polarization in Si II λ6355 is larger by ∼ +50 per cent at $\theta \approx +35^{\circ}$, vanishes at +90°, and becomes small for negative angles depending on the phase, whereas the overall level of p peaks at $\theta \approx +10^{\circ}$.

Downloaded from https://academic.oup.com/mnras/article/520/1/560/6988185 by University of Sheffield user on 26 May 2023

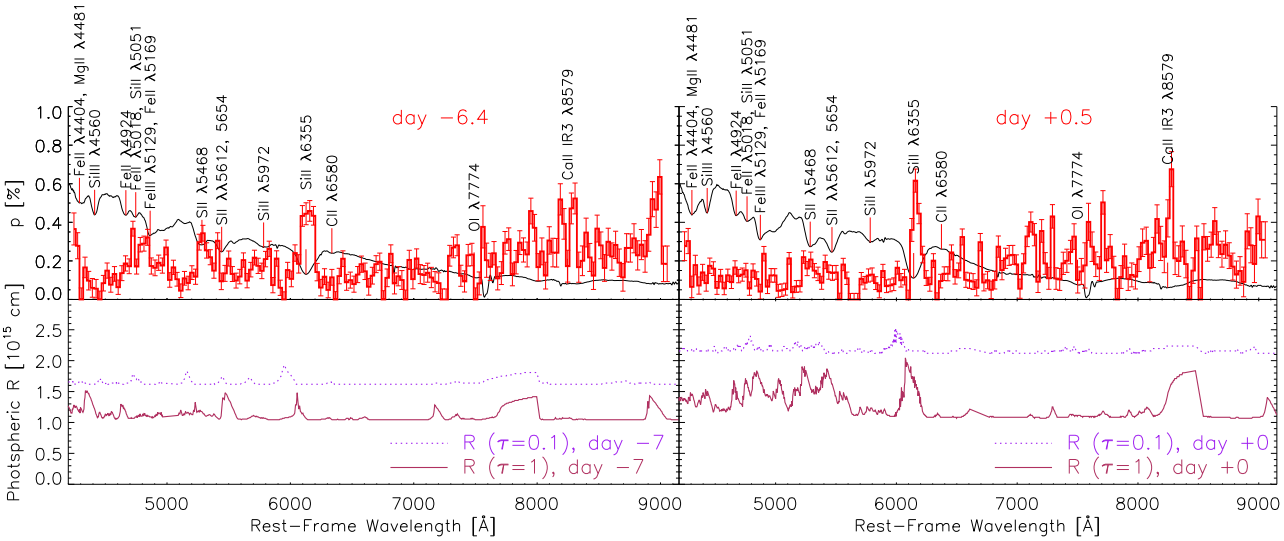

Figure 14. Flux and polarization spectra observed in SN 2019np compared to the spectral formation radius computed with Model 25. *Top panels:* Scaled flux spectrum (black curve) and degree of polarization (red histogram) observed on days −6.4 (left), and +0.5 (right). *Bottom panels:* Photon-decoupling radius R for $\tau = 0.1$ and 1 computed with delayed-detonation Model 25 at similar phases (left-hand panel for day −7 and right-hand panel for day +0). Major spectral lines are labelled. Note that the polarization is mostly produced by Thomson scattering between $\tau = 0.1$ and 1. Even strong features such as Si II λ6355, the Ca II NIR3 complex, and various blended features below 5500 Å are formed in the same region, setting a qualitative limit to the picture of line polarization being produced by chemically selective blocking of an underlying scattering-dominated photosphere.

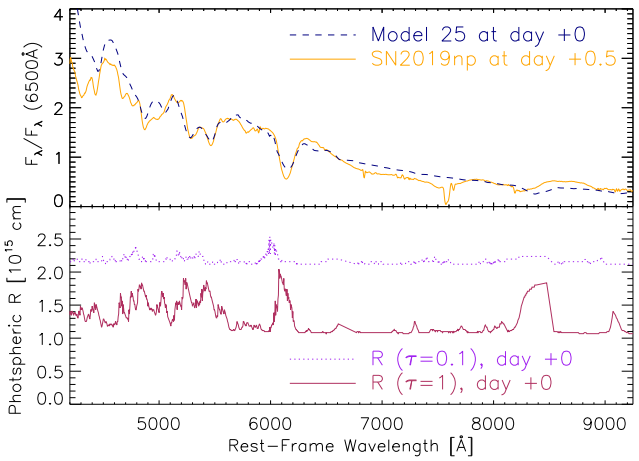

Figure 15. Spectral formation as a function of radius at maximum light. We compare the observation with the spectrum of Model 25 (upper panel) and the radii corresponding to optical depths of 0.1 and 1, between which the absorption features and the polarization are formed (Fig. 12). The observed and synthetic spectra generally agree without fine tuning. For strong lines like Si II λ6355, the flux minima and the blue wings typically correspond to an optical depth of 1 and 0.1, respectively. This is also true for other strong features such as Ca II NIR3 at ∼8200 Å and many of the line blends below 5500 Å. Strong spectral features form in the same region where the continuum polarization is also produced. The high-frequency structure in the radius of formation of Si II λ6355 is due to Fe II transitions which do not appear in the flux spectra, but show up in the line profiles as discussed in Fig. 16. Note the reduced effect of the quasi-continuum, justifying the wavelength range used for the determination of $p^{\rm cont}$ in Section 3.2.

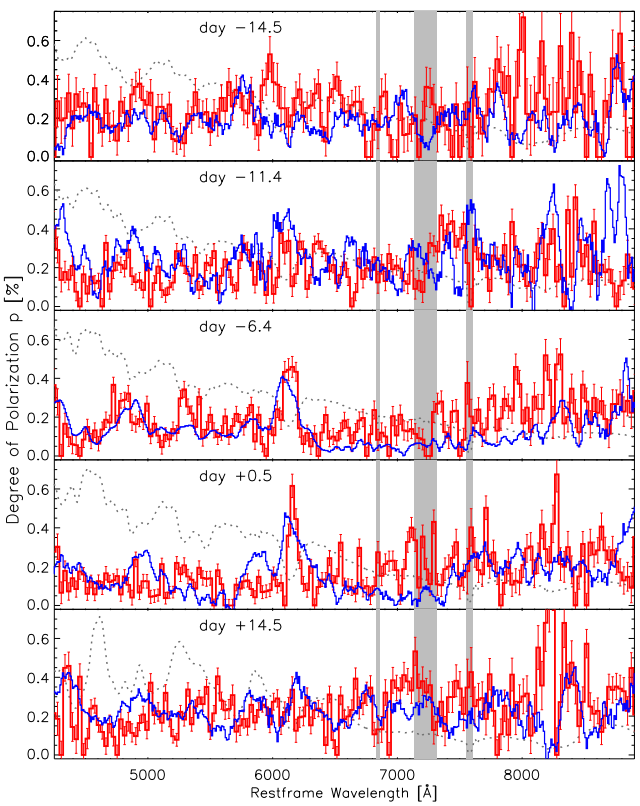

Figure 16. Polarization calculated with off-centre DDT Model 25 (blue histograms) compared to the intrinsic polarization of SN 2019np (red histograms) from days −14.5 to +14.5. The grey-dotted curve in each panel shows the observed scaled flux spectrum at the given epoch. In the model calculations, an inclination of ∼45° was adopted.

Downloaded from https://academic.oup.com/mnras/article/520/1/560/6988185 by University of Sheffield user on 26 May 2023

blend at ∼5800 Å, for which the simulations mostly reproduce the observations but on day +0.5. Both features can be identified as an elevation in the radius of photon decoupling as shown by Fig. 14. For these examples, the time to toggle from high to low polarization can be estimated from the rate with which the photosphere recedes over the abundance gradients. The gradients typically extend over ∼500–1000 km s^{-1} (Fig. 11) and so correspond to a time-scale of ∼1 day. From spectral analysis, a similar time-scale of a few days is well established for changes in ionization stages (Branch et al. 1981; Mazzali et al. 1993; Höflich 1995c; Lentz et al. 2001; Baron et al. 2006; Dessart et al. 2014). This is faster than our observing frequency of SN 2019np and may reflect an insignificant phase shift in the evolution of the models relative to the observations. This phase shift may also point toward small-scale structures such as Rayleigh–Taylor fingers or Kelvin–Helmholtz instabilities not included in our models, which would reveal themselves in short-term variations in the polarization spectra, but are not resolved in our data set. The numerous wiggles (Section 3.3 and Fig. 16) are not resolved in the current observations. They may possibly be understood in the same way as resolved features: namely in terms of atomic physics. Many coincide with features produced by the model. Some of them may indicate genuine small-scale structures, and others may be just noise in the data or ejecta. Their true nature cannot be determined with the current observations. This ambiguity points towards a need for high-cadence observations to separate small scale instabilities from imprints governed by atomic physics.

The change of the polarization profiles of (for example) Si II λ6355 can also be understood within the same framework, leading to a new diagnostic (Figs 14 and 16) of substructures in lines, although the spectral resolution of our polarimetry may not be sufficient to fully reveal the underlying velocity structure. Overall, the location of the peak (its Doppler shift) agrees between observations and synthetic profiles including the evolution of the line width. This supports the interpretation by large-scale asphericity in the abundance distributions. From the models, this evolution can be understood even though, at higher granularity, some discrepancies need to be discussed. (a) Binning of the data may introduce artifacts, in particular at very early times when the SNR is low in the current data as on day −14.5[9] or on day +0.5, when the polarization peak in Si II λ6355 occupies just one wavelength bin whereas the associated change in the position angle takes place over three bins (Fig. 4). (b) Some discrepancies between observations and model profiles may also hint at the model Fe opacities being too weak between 6000 and 6500 Å, possibly owing to a lack of Rayleigh–Taylor mixing, too low excitation of the atomic levels, or slightly too low a metallicity in the progenitor. As discussed above, even the strong lines are blended with many weak lines, which do not appear in the flux but in the polarization.

In the simulations, the strength of the polarization depends on the thermalization depth in the atmosphere and the density profile (see Section 4.2). If at some wavelength the thermalization depth is close to the Thomson optical depth of 1, the polarization peaks at that wavelength. It becomes smaller with decreasing thermalization depth and reaches the asymptotic value for large depths. As a result, the line profile is broader at early times when, owing to steep density profiles combined with decreasing abundances in the region of incomplete oxygen burning, namely around day −11.4, the radii of the photon decoupling regions are similar and, thus, the resulting profiles are broad. With time, the density slope flattens and, to first order, the profile becomes narrower. Note that, in an expanding atmosphere, the absorption is determined by the Sobolev optical depth which is not inherently spherically symmetric in wavelength (see Fig. 14). By days −6.4 and +0.5, the Si profile is formed in the QSE region and a flat density gradient leads to an increasing blueshift of the peak.

On day −11.4, Si II λ6355 is blended with Fe II λλ6293, 6358, 6497 and weaker Fe II and Fe III transitions from excited levels, leading to a more complicated profile. In the models, the iron blends seem to be weaker than in the observations. Because line absorption depolarizes, this can explain the lack of depolarization in the model profile in both the blue and red. For the same reason, at days −6.4 and +0.5, the observed profile has a steep decline whereas the synthetic profile shows a long red tail. The imprint of Fe II λ6497 may be seen in the observations. A similar shape of the Si II λ6355 polarization profile has also been seen in SN 2018gv around peak luminosity (Yang et al. 2020).

In the models and the observations after peak luminosity of SN 2019np, Si II λ6355 becomes progressively blended with several strong Fe II lines. The Si line has vanished by day +14.5 as the photosphere recedes into the NSE region, which displays strong Fe-group elements that form both a quasi-continuum and discrete lines in the spectrum. The feature at ∼6200 Å, which is conventionally attributed to Si II λ6355, becomes increasingly dominated by Fe II lines and, as a consequence, the corresponding polarization across this wavelength range also disappears. Overall, the quasi-continuum on day +14.5 is produced by numerous overlapping Fe-group lines from Fe, Co, Ni, etc.

Without fine-tuning of our model, the polarization spectra across several major spectral features can also be reproduced and generally agree with the observed polarization spectra (see Fig. 16). For the calculation of the continuum polarization, we use the wavelength range 6400–7000 Å applied in Section 3.2. The global asphericity in the electron density distribution on day −14.5 is not accounted for in the hydro simulation. Therefore, we imposed an overall elliptical distribution with an axis ratio of 2 to obtain the overall level of the polarization over the entire wavelength range observed (see Section 4.1). The choice of the axis ratio is motivated by Fig. 12 and results quantitatively from the most likely viewing angle, $\theta \approx 45^\circ$ (Section 4.3) and the relation $p \propto \sin^2\theta$ (Section 4.2).

At all later epochs, the continuum polarization is calculated directly without modifying the hydro model (Section 4.1). The continuum polarization produced by the detailed off-centre model (Fig. 16) is within the 1σ error range of the observed values (Table 2). On day −11.4, the asphericity in the electron density is caused by the aspherical abundance distributions.[10] Its value is ill-defined because of steep changes of the synthetic polarization at the edges of the 6400–7000 Å wavelength range (see the second panel from top of Fig. 16), although we used the same range as in Section 3.2 to minimize the effect of lines. Therefore, the value of 0.16 ± 0.04 per cent returned by the models is somewhat larger than the observed level of 0.099 ± 0.080 per cent, but well within the error range. The synthetic continuum polarization on days −6.4, +0.5, and +14.5 are 0.05 per cent(0.075 ± 0.080 per cent),

[9]On day −14.5, Si II λ6355 shows multiple components at 25 Å binning.

[10]In SNe Ia and unlike SNe II, the resulting asphericity in the electron distribution remains rather small, 5–10 per cent, because the free electrons per nucleon are about equal for Si/S II and Fe/Co II-III. For example, in the hydrogen-rich envelope of SNe IIP, the opacity drops by 4 orders of magnitudes over the recombination front of hydrogen, causing highly aspherical Thomson-scattering dominated photospheres even in case of slightly aspherical ^{56}Ni distributions or rotation (Höflich, Khokhlov & Wang 2001; Leonard & Filippenko 2005).

Downloaded from https://academic.oup.com/mnras/article/520/1/560/6988185 by University of Sheffield user on 26 May 2023

0.06 per cent (0.110 ± 0.100 per cent), and 0.22 per cent (0.186 ± 0.104 per cent), respectively, with the observed values given in brackets.[11]

Most of the discrete polarization features are at the level of ≲ 0.2–0.4 per cent. In the models, they are produced by depolarization or the frequency variation in the thermalization optical depth. Whether they appear as local maxima or minima in the polarization spectrum depends on the scattering optical depth of the corresponding region of formation. Many of these wiggles in the observed polarization spectra (Section 3.3) coincide with features in the synthetic polarization spectra. Discrepancies may be due to small-scale structures that the observations of SN 2019np do not resolve in time and wavelength. This may hint at the possibility of significant detection of numerous weakly polarized lines in future higher SNR observations with FORS2 at ESO's VLT. Since some patterns do not have mutual counterparts, such observations should also aim for higher spectral resolution. Simulations with matching resolution are feasible with moderate additional effort (see Section 6.1).

Although our models reproduce many (even relatively minor) aspects of the observations, some limitations are also apparent. For instance, on day −14.5, the synthetic polarization spectra exhibit fairly similar overall patterns, but the models do not show the large-amplitude fluctuations with wavelength observed in the polarization spectra of the strongest resonance lines, namely in Ca II NIR3 (see Fig. 8 and Section 3.4) and possibly in Si II λ6355.[12] The involvement of Ni, Co, or Fe seems to be ruled out because, in the spectral region strongly affected by iron-group elements ($\lambda \lesssim 4700$ Å and $\lambda \gtrsim 8500$ Å), similar patterns do not exist and observations and synthetic spectra agree well for our model with solar abundances in the outer C/O layers and Fe, Co, and Ni mass fractions of 0.002, 0.00005, and 0.0001, respectively (Anders & Grevesse 1989). As discussed in Section 6.1, an amount of $M(^{56}\mathrm{Ni}) \approx 0.02$–$0.03\,\mathrm{M}_\odot$ in the outer $0.2\,\mathrm{M}_\odot$ (∼0.1 in mass fraction; alternatively produced in a sub-M_{Ch} explosion) is needed to explain the early bumps in light curves of SNe 2017cbv and 2018oh. The associated spectra are dominated by Fe, Co, and Ni lines (Höflich 1998; Magee & Maguire 2022), traces of which are likely just barely seen in all spectra of SN 2019np (Fig. 16).

Another example for the shortcomings of our current model is the increased polarization in Ca II NIR3 around and after maximum light, which is not reproduced by our models. This resonance line has by far the largest cross-section and is optically thick even in regions with solar abundances, so that very minor inhomogeneities can have a big impact on the polarization. Extended, inhomogeneous radial components in the Ca distribution may be expected from Rayleigh–Taylor instabilities, interactions with a companion star, and/or sheet-like/caustic structures, which may develop within 5–10 d after the explosion as the result of mixing of radioactive ^{56}Ni and electron-capture elements (Marietta, Burrows & Fryxell 2000; Fesen et al. 2007; Hoeflich 2017; Maeda et al. 2018). Additionally, the late rise of the Ca II NIR3 polarization may also be caused by the alignment of calcium atoms in the presence of a magnetic field as recently suggested by Yang et al. (2022). If combined with near- and mid-infrared nebular spectra, later-epoch polarimetry of the Ca II NIR3 feature will allow us to discriminate between various possibilities concerning the nature of the progenitor and the explosion mechanism as discussed by Höflich et al. (2004), Telesco et al. (2015), Hoeflich et al. (2021), and Ashall et al. (2021), since the spatial distribution of radioactive Co and stable Fe, Ni, and Co can be probed independently.

4.4 SN 2019np in polarimetric context with other Type Ia SNe

The polarization properties of some Type Ia SNe are remarkably different from those that are typical for normally bright thermonuclear SNe (Cikota et al. 2019; Patra et al. 2022) and SN 2019np. An example is SN 2004dt, which exhibited exceptionally high polarization in some spectral lines. For instance, the peak polarization across Si II λ6355 reached ∼2.4 per cent and ∼3 per cent after binning to 50 Å and 25 Å, respectively (Wang et al. 2006; Cikota et al. 2019). Although the continuum polarization was as low as ≲0.2–0.3 per cent around peak brightness (Leonard et al. 2005; Wang et al. 2006), many features of Si, S, and Mg in the synthetic polarization spectrum[13] had their equivalent in the observations (Höflich et al. 2006b) as commonly found in Type Ia SNe. These findings might be accounted for by either a violent merger of two C–O WDs (Bulla et al. 2016a) or an off-centre delayed detonation model within a continuum of parameters consisting of especially the position of the delayed-detonation transition, the amount of burning during the deflagration phase, and the viewing angle of the observer (Höflich et al. 2006a).

For normally bright Type Ia SNe, the polarization of Si II λ6355 5 d before *B*-band maximum light ($p_{\mathrm{Si\,II}}^{-5\,\mathrm{d}}$), which is representative of the maximum value ($p_{\mathrm{Si\,II}}^{\mathrm{max}}$), correlates with the light-curve stretch parameter measured as the decline in magnitude within 15 d after *B* maximum [$\Delta m_{15}(B)$; Wang, Baade & Patat 2007; Cikota et al. 2019]. For SN 2019np, Sai et al. (2022) measured $\Delta \mathrm{m}_{15}(B) = 1.04 \pm 0.04$ mag, and $p_{\mathrm{Si\,II}}^{\mathrm{max}}$ amounted to 0.62 ± 0.03 per cent on day +0.5 (with 30 Å binning; Fig. 9). Therefore, we conclude that SN 2019np is consistent with the $p_{\mathrm{Si\,II}}^{\mathrm{max}}$–$\Delta m_{15}(B)$ relation.

In a follow-up study, Maund et al. (2010b) investigated Si II λ6355 observations of a sample of nine normal Type Ia SNe and found that $p_{\mathrm{Si\,II}}^{-5\,\mathrm{d}}$ is also correlated with the temporal velocity gradient $\dot{v}_{\mathrm{Si\,II}}$. Accordingly, the deceleration of the SN expansion is also correlated with the degree of chemical asphericity. The interpolated velocity gradient of SN 2019np was $21 \pm 5\,\mathrm{km\,s^{-1}\,d^{-1}}$ on day +10 (Sai et al. 2022). By interpolating the Si II λ6355 velocity evolution estimated from our VLT observations, we estimated velocity gradients of 53 ± 19 and 22 ± 9 $\mathrm{km\,s^{-1}\,d^{-1}}$ on days +0 and +10, respectively. This means that SN 2019np was also consistent with the $p_{\mathrm{Si\,II}}^{-5\,\mathrm{d}}$–$\dot{v}_{\mathrm{Si\,II}}$ relation.

Subluminous Type Ia SNe exhibit substantially different polarization properties than discussed above. For instance, a polarization of ∼0.7 per cent in the optical continuum but only ∼0.3 per cent across Si II λ6355 were observed in SNe 1999by (Howell et al. 2001) and 2005ke (Patat et al. 2012) at ∼0 and −7 d relative to maximum light, respectively. The high degree of continuum polarization can be explained by a global asphericity of as much as 15 per cent (Patat et al. 2012). These two events are outliers from the correlation proposed by Wang et al. (2007) between the Si II λ6355 polarization 5 d before *B*-band maximum and Δm_{15}, nor do they match the relation between the velocity gradient of Si II λ6355 and the associated peak polarization

[11]Note that the variations in the observed continuum polarization are on a 2σ level (Section 3.1). However, they also coincide with a change in the dominant axis in the *Q*–*U* diagram (Fig. 7), and σ includes spectral variations by lines.

[12]On day −14.5, the feature at ∼6000 Å (within the Si II λ6355 profile, Fig. 16), which occupies a single bin with 30 Å binning, breaks up into two components with peaks at 0.48 per cent and 0.39 per cent if 40 Å bins are used.

[13]The continuum polarization in the off-centre DDT is ∼0.1–0.2 per cent.

Downloaded from https://academic.oup.com/mnras/article/520/1/560/6988185 by University of Sheffield user on 26 May 2023

(Maund et al. 2010b). The mismatch may be due to SNe 1999by and 2005ke perhaps being typical representatives of underluminous Type Ia SNe. Their spectroscopic and polarimetric properties can be understood within the frameworks of delayed detonations originating from a rapidly rotating WD or WD–WD mergers (Patat et al. 2012).

5 CONCLUSIONS

At five epochs between d −14.5 and +14.5 from maximum light, we have obtained high-quality optical VLT spectropolarimetry of the normal Type Ia SN 2019np. The first epoch of our observation is the earliest such measurement carried out to date for any Type Ia SN. The data have been analysed with detailed radiation-hydrodynamic non-LTE simulations in the framework of an off-centre delayed detonation which produces aspherical distributions in the burning products and, in particular, an aspherical ^{56}Ni core. The observations are also compatible with the presence of a central energy source that deviates from spherical symmetry. The understanding of SN 2019np that we have achieved with our simulations can be summarized as follows:

(1) A viewing angle of ∼45° provides the best fit to the amplitude and temporal evolution of the polarization spectra including Si II λ6355 and the continuum (Section 4). As discussed in point (3) below, the continuum polarization at the first epoch on day −14.5 requires a separate component.

(2) The five epochs roughly cover the time interval in which the photosphere receded through the layers of incomplete carbon burning, complete carbon burning, incomplete and complete (QSE[14]) explosive oxygen burning, and incomplete Si burning at the interface to NSE. The cadence of the observations corresponds to a resolution of ∼6000 km s^{-1} in expansion velocity. Higher-cadence observations than obtained for SN 2019np are required to resolve any structures in the ejecta at smaller scales. For instance, considering the stratification in expansion velocity of the abundance layers and the recession speed of the photosphere, a cadence of ∼1 day would be essential to map out the interfaces between different chemical layers.

(3) The outermost $\lesssim 4 \times 10^{-3}$ M$_\odot$ region seen during the first ∼3.5 d after the SN explosion is consistent with a C/O-rich layer. The change of the polarization position angle (Fig. 7) and the rotation of the dominant axis (Fig. 8) from the first to later epochs suggest a different orientation of the outermost layer compared to the inner regions. To account for the outer asymmetry, a separate structure had to be added to the models. This renders it relatively unlikely that SN 2019np originated from a sub-$M_{\rm Ch}$ double detonation induced by a helium shell at the surface of the WD because the initial shape of the core of the WD can be expected to be symmetric, being governed by gravity. A deformation of the core may occur in a rapidly, differentially rotating WD with extreme specific angular momentum close to the centre (Eriguchi & Mueller 1993), but is not likely.

(4) Although the continuum polarization on day −14.5 was only 0.21 per cent±0.09 per cent, the hydrodynamic modelling of the polarization with an evolving density profile suggests the presence of a remarkably aspherical outermost layer of the SN, comprising a fraction of $\sim(2\text{–}3) \times 10^{-3}$ of the WD-progenitor mass. In conjunction with the inclination of ∼45°, the axis ratio of the electron density distribution predicted by the models amounts to ∼2–3. That is, in the presence of a steep density gradient in the outermost layers, a low but non-zero continuum polarization cannot be taken as an indicator of a high level of sphericity.

(5) The rise of the continuum polarization to 0.19 ± 0.07 per cent about two weeks after peak luminosity is consistent with an aspherical ^{56}Ni distribution in the core as predicted by off-centre delayed-detonation models. From the models, a change of the polarization position angle by ∼20° can be expected. The time-evolving distribution of the polarimetric signals in the polar plots (Fig. 8) and the rotating dominant axis on the Q–U plane (Fig. 7 and Section 3.3) are consistent with this prediction. Around maximum light, the off-centre contribution causes a continuum polarization of ≲0.1 per cent.

(6) Small $p^{\rm cont}$ seems to be a characteristic of off-centre DDT models. This justifies the assumption of negligible intrinsic polarization made for the determination of the ISP (Section 3.1). This method differs from those commonly applied to core-collapse SNe (Section 3.1). The difference between the continuum polarization $p^{\rm cont}$ and the average polarization over the entire spectrum with many line-dominated spectral regions remains small, ∼0.1 per cent from −6.4 to + 0.5 d for our normally bright off-centre DDT model. The difference is consistent with the observations of SN 2019np. To understand the physical reason for being small, see Section 4.3. Despite much stronger line polarization, a similar small value of $p^{\rm cont}$ and a small difference in the continuum is found for the Type Ia SN 2004dt when analysed within the framework of off-centre DDT models (Section 4.4).

(7) The polarization observed across Si II λ6355 on day −14.5 is higher than in our model (Fig. 16). The dominant axes fitted to this line and the optical continuum are both not well defined at this phase (Section 3.3). From our full-star models, it is hard to deduce whether the asphericity of these two components in the outermost layers has a common origin – for instance, owing to interaction with a low-mass accretion disc, which is a free parameter and remains unconstrained in the current modelling process of the full star. However, the toy model for the continuum polarization (Section 4.2) demands different symmetry axes for the density and the abundances.

(8) High asphericity is found to be confined to the very outer layers. It emerges from the fitting when introduced as an additional free parameter not included in the hydrodynamical model. Possible physical causes may include a short-lived interaction between the SN ejecta with a low-mass accretion disc (Gerardy et al. 2007) or a companion star (Marietta et al. 2000), or surface burning as found in sub-$M_{\rm Ch}$ explosions (Shen et al. 2012) but see item (3), or the imprint of the burning of H/He-rich material originating from the surface (Hoeflich et al. 2019). Interaction with a donor star seems less likely because it would affect not only the outermost layers. As shown in Figs 1 to 3 and discussed in Section 4, the sub-$M_{\rm Ch}$ model is in tension with the observation of the Ca II NIR3 feature. A similar early-time polarization has been observed in the normal-bright SN 2018gv (Yang et al. 2020). However, in the underluminous SN 2005ke, a significant polarization was observed in the outer ∼0.2 M$_\odot$, hinting toward rapid rotation or a dynamical merger (Patat et al. 2012).

(9) The continuum polarization of SN 2019np vanished by day −11.5 and remained consistent with zero within one σ until the SN reached its peak luminosity, indicating a high degree of spherical symmetry between the outermost 0.02–0.03 M$_{\rm WD}$ and ∼0.5 M$_{\rm WD}$. In the case of a highly aspherical configuration extending into deeper layers, the continuum polarization should increase with time since the density distribution flattens significantly and the scattering optical depth decreases from the optically thick regime. However, such an increase in continuum polarization was not observed in

[14]QSE: Quasi-Statistical-Equilibrium.

Downloaded from https://academic.oup.com/mnras/article/520/1/560/6988185 by University of Sheffield user on 26 May 2023

SN 2019np. This partly invalidates the conventional assumption that a low continuum polarization provides evidence of low asphericity. In the presence of a steep density gradient as in the outermost layers of SN 2019np, major deviations from spherical symmetry are well possible. High-cadence observations are needed to distinguish between these alternatives.

(10) The increased continuum polarization on day +14.5 can be explained by abundance asphericities in an off-centre delayed detonation. The direction of the dominant axis of SN 2019np has also changed between days +0 and +14.5 (Fig. 7), which may indicate a small, off-centre distribution of the central energy source, 5–10 per cent of the total amount of ^{56}Ni. The model also predicts a change of the polarization position angle of the quasi-continuum. Although qualitatively indicated by the observations, the change in the polarization position angle of the continuum is hard to quantify from the available observations because the intrinsic continuum polarization is very low (Section 3), and the numerous small wiggles at this low level may also cause a problem (Figs 14–16).

(11) None of the possible mechanisms causing the rise of the Ca II NIR3 polarization on day +14.5 has been included in our simulations. Its origin remains uncertain, as discussed in Section 4.3.

(12) In the optical domain, spectral line formation and polarization by electron scattering take place in the same region of the expanding atmosphere (Section 4.3 and Fig. 15). By contrast, the canonical polarization-by-obscuration picture (Wang & Wheeler 2008) requires that spectral lines are formed mainly above the last continuum-scattering surface. To first order, this approximation can be used to place an upper limit on the peak polarization from large-scale asymmetries, which are produced by the large Sobolev optical depth over the entire photosphere, if the formation of the quasi-continuum is dominated by Thomson scattering. In SNe Ia, the Si II λλ6348, 6373 doublet provides an example. It originates from a low-excitation state, and Si accounts for ∼60 per cent of the total mass fraction corresponding to up to ∼2500 times the solar value found in the H-rich envelopes of CC-SNe. The expansion velocities of Si-rich layers range from ∼9000 to more than 22 000 km s^{-1}. In the presence of large-scale asphericity in Si, this line will be significantly polarized unless the region of asymmetric density or Si abundance is hidden behind an extended photospheric region. For small-scale or multiple structures, the resulting polarization depends sensitively on τ_{sc} at their location.

(13) Overall, the polarization spectra and their temporal evolution can be understood as a variable thermalization optical depth and partial blocking of the photosphere at a given geometric depth.

(14) There are strong high-amplitude fluctuations in the polarization spectra on day −14.5. They can be attributed to the strongest S/Si and the Ca II lines, in particular Ca II NIR3. The lack of similar patterns and the agreement between the observations and synthetic spectra in the spectral region dominated by iron-group elements, namely the *U* and *B* bands and longwards of 8500 Å, seem to rule out Ni, Co, or Fe as being affected by the same mechanism(s) responsible for the fluctuations just mentioned. For details and their possible origin, see Section 4.3.

(15) At the same time, there are also flocculent structures in the polar diagram for Ca II NIR3 (Section 3.4, Fig. 16) with a broader distribution in position angle and a lower polarization degree (see Fig. 8), suggesting a more complex structure of the outermost layers than adopted in the models.

(16) Many relatively weak polarization features within the wavelength range ∼4500–6000 Å and beyond 6800 Å can be interpreted as signatures of spectral-line blends and unresolved wiggles. The general agreement between data and model suggests that many of these weak polarization features are real. Some discrepancies do not necessarily invalidate this conclusion, but likely point toward small-scale structures (Section 4.3). However, the noise in the data for SN 2019np sets a limit to probing those scales in this event.

(17) Polarization is able to pick up spectral signatures not visible in the flux spectra because lines depolarize but both absorb and emit photons (see Section 4.3). Spectropolarimetry of sufficient spectral resolution can reveal spectral lines that are undetectable in flux spectra, and, at proper cadence, their depth of formation can be inferred. This added diagnostic power is independent of any asphericity and can be important to discriminate explosion scenarios.

(18) The asphericity in the ^{56}Ni distribution is significant (Fig. 11) although the continuum polarization is relatively low. As discussed in Section 4.2, a low thermalization depth results in vanishingly low continuum polarization, except for photons that graze the photosphere at low optical Thomson-scattering depth (see Section 4.3). As a corollary, high polarization can be expected if the off-centre component dominates, but polarization may fail to detect even significant asphericity in the density produced by a Fe/Co/Ni core.

(19) The polarization profiles of strong isolated features provide new diagnostics to probe for mixing on small and medium scales, and to explore the chemical stratification (Section 4.3).

6 FUTURE OPPORTUNITIES

6.1 The diagnostic power of spectropolarimetry of Type Ia SNe

Asphericity holds a key to the understanding of the nature of thermonuclear SNe. It involves three main components: (1) the exploding WD, (2) all other matter bound in the progenitor system, which may include a companion star and any bound CSM such as a common envelope or an accretion disc, and the inner parts of several winds (e.g. from the WD, a companion star or its Roche lobe, and an accretion disc), and (3) the unbound CSM consisting of the outer faster and less dense parts of the winds and ultimately the interstellar medium.

A detailed discussion of the effects of these three constituents on the geometry is beyond the scope of this paper. A broad introduction to the geometrical signatures in polarization and nebular spectra expected from all commonly considered explosion models and progenitor channels was recently given by Hoeflich et al. (2021). Reviews on various topics can be found among the articles collected in Alsabti & Murdin (2017):

(a) To properly plan observing sequences, time-scales are critical. For all explosion paths, the initial phase of the explosion takes a few seconds to a minute, and the main spatial dimension is given by the exploding WD or the two merging WDs and ranges from 1.5×10^8 to 10^9 cm. The hydrodynamical interaction of the explosively expanding envelope with a companion star, any accretion disc, and the inner parts of the wind(s) takes place within ∼10^{10}–10^{13} cm. Considering the velocities and masses in the outer layers of the explosion, this corresponds to time-scales of minutes to about an hour for interaction with the bound matter. Interaction with the wind(s) and the ISM can extend over days to many years, and is only limited by the transition to the SN-remnant phase.

(b) The impact of the various components on the geometrical structure and the associated polarization depends on the mass of the companion and any bound CSM relative to that of the ejecta which differs strongly between the explosion processes (∼0.6–2 $M_\odot$).

(c) The mass-loss rate from the system may range from ∼10^{-6} to 10^{-4} $M_\odot$ yr^{-1} and can be due to any model-dependent combination of

Downloaded from https://academic.oup.com/mnras/article/520/1/560/6988185 by University of Sheffield user on 26 May 2023

the wind from the WD, the wind from a companion, super-Eddington accretion on to the WD (e.g. Nomoto, Sugimoto & Neo 1976), the Roche lobe in a single-degenerate system, or the high-velocity wind from accretion discs in cataclysmic variables, or it may be produced during the final phase of dynamical mergers. Upper limits to the total mass content of these winds integrated over the time considered for early polarimetry are $\sim 10^{-4}$–10^{-7} $M_\odot$ (Dragulin & Hoeflich 2016; Chevalier & Fransson 2017). Even at the earliest times when significant polarization can still be expected, the dynamical effects of the impact of the ejecta on the unbound CSM are likely to be small (Fig. 11). Nevertheless, in early-time photometry, some small additional blue flux may appear owing to energy released during the interaction. For very high wind densities, the hard radiation at the shock discontinuity and the reverse shock may lead to enhanced ionization in the photosphere of the SN. In SN 2019np, we see no obvious evidence of such effects (Section 4.3).

(d) The CSM bound in the system may include matter in a Roche lobe and/or an accretion disc. Observational evidence has been reported by (for example) Aldering et al. (2006), and, from high-velocity Ca II absorptions in early-phase spectra, its mass has been estimated to be of order 10^{-2}–10^{-3} $M_\odot$ (Gerardy et al. 2007). This mass is comparable to that in the layers probed by our early polarimetry of SN 2019np, and it is compatible with the large asymmetries proposed (Fig. 11). The small-scale structures depend on the scale height of the material (e.g. the Roche lobe or the disc) and the sound-crossing time during the hydrodynamical phase of the interaction. However, since the mass of the bound CSM is much larger than that contained in the wind, the structure produced by the interaction of the ejecta with this matter can be expected to be conserved in the subsequent possible interaction with the outer winds and the ISM, although the temperatures and sound speed are likely to be high (Margutti et al. 2014; Hsiao et al. 2020). Therefore, polarimetry will provide a unique way to explore the bound CSM. As discussed above (Sections 3.3 & 4.3), some of the wiggles in polarization spectra and flocculent structures in polar plots seen in the spectropolarimetry of SN 2019np may have their origin in Rayleigh–Taylor or Kelvin–Helmholtz instabilities and crossing shock waves produced during the injection with an orientation imprinted by the bound CSM. Polarization measurements with a latency between hours and one day are needed (Fig. 17) to learn whether the polarization position angle persists, which would suggest a large-scale structure, dominated by instabilities imprinting their characteristic size as wiggles and large-amplitude fluctuations in the polarization spectra as well as flocculent structures in the polar diagrams, or a combination of large and small scales. These structures become most prominent in Ca II NIR3, which is an excellent tracer of structure owing to its large atomic cross section.

(e) Alternatively, the early wiggles and the flocculent structures in SN 2019np may be related to the explosion mechanism, in which case they would have an origin internal to the SN proper. Potential sources are explosive surface He-burning in sub-$M_{\rm Ch}$ explosions (e.g. Shen & Moore 2014) or in NSE-rich material rising from the central region in gravitationally confined thermonuclear explosions (Kasen & Plewa 2005). In both cases, some 0.02–0.1 $M_\odot$ of ^{56}Ni may reach near-surface regions. This is well within the mass range that can be probed by polarization as in SN 2019np (Fig. 11) because the characteristics and especially the structures associated with these processes are different. A central distinguishing criterion is the presence of products from low-density burning in sub-$M_{\rm Ch}$ explosions and of NSE-dominated material from high-density burning and a mixture of NSE and QSE in gravitationally confined detonations.

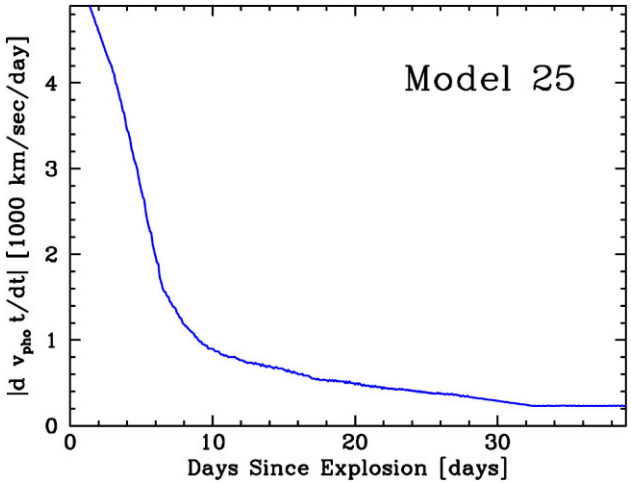

Figure 17. Rate of recession of the photosphere in the spherical high-resolution Model 25 as a function of time. The recession rate $dv_{\rm phot}/dt$ for Model 25 (see Section 4) was calculated using the Rosseland mean opacity in the optical and a range of ±2 d to determine $v_{\rm phot}$. The exact values depend on the explosion model used (see fig. 9 of Quimby et al. 2007).

Prompted by detections of early excess luminosity in optical light curves, Piro & Kollmeier (2018) suggested ^{56}Ni as a possible energy source. At a first glance, early photometry of iPTF16abc (Miller et al. 2018) and SN 2019np (Sai et al. 2022) makes it plausible that both light curves can be well explained by ^{56}Ni mixed into the outer layers of the ejecta. A more detailed study has been presented by Magee & Maguire (2022). The authors proposed that the bump in the light curve can be understood by a Ni shell of 0.02–0.03 $M_\odot$ in the outer 0.2 $M_\odot$ but also noted that the colours are too blue, and the spectra would be dominated by Fe/Co/Ni. Since both of these side effects are not supported by the observations, the authors suggested as a remedy that the inferred 10 per cent of ^{56}Ni is concentrated in a small clump. However, the observed flux and polarization spectra safely rule out ^{56}Ni-powered early-time light curves (Section 4.3). Moreover, the proposed small clump is unlikely to be the correct explanation; the luminosity would be dominated by a plume resulting in a flip in polarization position angle (Fig. 12) because even as little as 0.02 $M_\odot$ of ^{56}Ni would dominate the energy input. In both the sub-$M_{\rm Ch}$ and the gravitationally confined detonation, the hypothetical ^{56}Ni would be in the surface layer. It would contribute 50 per cent of the total heating and be equivalent to the energy output from 0.1 $M_\odot$ of ^{56}Co, and may not solve the blue-colour problem. The latter may be an opacity effect in a rapidly expanding atmosphere instead of a heat indicator (Ashall et al. 2022). The presence of burned material from a He-triggered sub-$M_{\rm Ch}$ explosion can be clearly demonstrable with spectropolarimetry because it can detect iron-group elements down to solar metallicity (Section 4.3), which is not possible from total-flux spectra alone. Furthermore, polarimetry is the ideal tool to distinguish explosions without surface burning and He-triggers in sub-$M_{\rm Ch}$ WDs.

(f) Interaction of the SN ejecta with a companion star is a consequence of most explosion models except for the violent, dynamical, and secular mergers. The early bump identified in the photometry of SN 2017cbv appears blue and has been modelled by interactions with a subgiant star at a distance of 56 solar radii from the exploding WD (Hosseinzadeh et al. 2017). However, the model also predicts a stronger ultraviolet flux than was observed. All SN mechanisms with an internally triggered explosion seem to have a problem explaining the early blue excess flux and for the explanation

Downloaded from https://academic.oup.com/mnras/article/520/1/560/6988185 by University of Sheffield user on 26 May 2023

to resort to interaction with some CSM. An interaction with a relatively high-mass object can be expected for many progenitor systems, and it would leave its imprint not only in the surface layer but all the way down to the central region. So large a structure is likely to become visible in polarization. But it may also produce small-scale structures in the abundances and, depending on the donor star, the density (Marietta et al. 2000). Interaction with a companion causes a tight connection between outer and inner regions of the expanding envelope, including a common and persistent symmetry axis and, initially, a cone with an opening angle of $\sim 30^\circ$. Although our modelling of SN 2019np did not include a companion, the observed change in polarization angle (Figs 1–4) probably disfavours a dominant effect of an ejecta/companion interaction on the polarization (Fig. 16). Any such effect depends on the size of, and distance to, the companion star, and the large-scale asymmetry imposed by a small companion can be expected to be largest in deep layers (Marietta et al. 2000). Furthermore, in contrast to an off-centre DDT, a small-scale structure produced by Rayleigh–Taylor instabilities will occupy a cone instead of a spherical layer. Unfortunately, in our study of SN 2019np, we lack the cadence to resolve small scales and their distribution from the outer to the inner regions.

(g) For deflagration fronts, we must expect small-scale Rayleigh–Taylor instabilities and the imprint of the thermonuclear runaway, the caustic distribution of the burning processes, and magnetic fields as discussed throughout this paper (especially Sections 4.3 and 5) and by Hristov et al. (2021). Polarimetry of Ca II NIR3 is a highly sensitive tool to probe for the associated structures. The polarization of this triplet in the central region is strong evidence for mixing from the outside because burning to hot NSE destroys Ca (Fig. 11). However, the huge atomic cross-section of Ca II NIR3 desensitizes it to abundance effects (Section 4.3). When observations of this feature and the continuum polarization with similar characteristics as ours of SN2019 np but with higher cadence are combined with high-resolution nebular spectra in the near- and mid-infrared at later epochs, a fairly complete three-dimensional model of the structure of thermonuclear SNe can be assembled (Kotak et al. 2004; Telesco et al. 2015; Hoeflich et al. 2021).

(h) Off-centre DDT explosions of $M_{\rm Ch}$ WDs can generally be thoroughly investigated by spectropolarimetry. For sub-$M_{\rm Ch}$ explosions, the location of the secondary ignition of the C/O core can only be expected to show an imprint on the polarization spectrum if it happens in the regime of distributed burning.

(i) For SN 2019np, we found evidence of an off-centre component in the ^{56}Ni distribution, which disfavours sub-$M_{\rm Ch}$ explosions. However, we also showed that large-scale asymmetries in the extended central Fe/Co/Ni region cannot be excluded (Section 4.2). Contrary to normal-bright SNe and SN 2019np in particular, polarimetry of underluminous Type Ia SNe provided strong evidence for significant asphericity even in deeper layers. This may favour fast rotating WDs or dynamical mergers (Section 5). A possible discriminator may be the presence of Rayleigh–Taylor instabilities in models with deflagration burning, and their absence in pure detonation models like dynamical mergers (García-Berro & Lorén-Aguilar 2017). As explained above, time-resolved polarimetry can establish the actual facts.

(j) The Introduction has discussed polarization of Type Ia SNe as a diagnostic tool, also in connection with minority events like violent mergers (Kushnir et al. 2013; Pakmor 2017). Such events should exhibit prominent polarization signatures because the off-centre component would dominate (Fig. 12). Therefore, the amplitude in the continuum polarization with time would be larger by a factor of 5–6, and large polarization can also be expected in spectral lines.

6.2 Implications for the design of spectropolarimetric observing sequences and simulations

Spectropolarimetry with adequate cadence from the earliest possible moment and (to potentially expose the EC layers) up to $\sim$3 weeks after maximum brightness is necessary to get a comprehensive picture of normal Type Ia SNe on all scales and to discriminate between competing interpretations. The SNR must be high, and the spectral resolution should be better than that of our SN 2019np data. In our observations of SN 2019np, the combination of a spectral resolving power of $R \approx 440$ and a $\sim$4–6 d cadence only achieved a resolution of $\sim$6000 km s^{-1} in comoving-frame velocity between mass elements. This limited our analysis of any smaller scale structure in the SN ejecta and the surface layer. Observations with low cadence disqualify for several quantitative comparisons with models, most importantly the identification of individual clumps (predicted by Rayleigh–Taylor instabilities), layers of specific chemical elements, the interface between the Ca-rich and the inner NSE-region (Fig. 11), and the origin of the asphericity in the outermost layers.

To devise a more optimized observing strategy, the evolution of the recession velocity of the photosphere needs to be considered, which Fig. 17 illustrates for Model 25. Starting $\sim$1 week after explosion, during the rising and photospheric phases of Type Ia SNe, this velocity declines from $\sim$1000 to $\sim$200 km s^{-1} d^{-1}. Accordingly, a 2–4 day observing cadence suffices to locate the interfaces between various chemical constituents relevant for the internal structure of the explosion (items (e)–(j) above and Fig. 11). With one-day cadence and a matching spectral resolving power of 1000 (corresponding to a transversal resolution of 300 km s^{-1}), the morphology and origin of the individual structures discussed in items (e)–(j) can also be explored, namely the properties of the burning front including secondary detonations or a DDT, shear instabilities due to interactions with a companion star, the imprint of the thermonuclear runaway, the consequence of mixing of radioactive and EC elements, and possibly magnetic fields.

To also determine the shape of the outermost layers of the exploding WD calls for rapid-response and high-cadence observations because the radial density index governing this shape changes early and rapidly. Some 3.5 d after the explosion, a one-day cadence corresponds to a radial resolution of $\sim$3500 km s^{-1} and 10^{-4} M$_\odot$ in mass (Fig. 11). Therefore, such observations resolve both the bound CSM [item (d) above] and the He layer and ^{56}Ni mass [item (e)] to be expected for sub-$M_{\rm Ch}$ or confined detonation models. At an expansion velocity of 24 000 km s^{-1} (a typical value of high-velocity components in Ca II NIR3 and the cut-off velocity of the blue wings in Si II λ6355; Gerardy et al. 2007; Quimby et al. 2007), the transversal resolution (which is set by the spectral resolution of 300 km s^{-1}) exceeds the radial resolution by a factor $\sim$10. These resolutions describe cones with approximate opening angles of 20° and 2° for the radial and transversal directions (respectively), and are respectively governed by the cadence and the spectral resolution.[15] The apices of the cones are at the centre of the WD and the numerical grid. The opening angles are comparable to the angle suspended by (for example) the region affected by an interaction with a companion star, or about 20 and 2 per cent of the photospheric radius.

With such data, the interaction of the ejecta with an accretion disc, a Roche lobe (item (d) above) and a progenitor star (item (f)) can be significantly distinguished. They may also be sufficient to

[15]The opening angles are given by the arcsin of the structure size divided by the photospheric radius in velocity space.

Downloaded from https://academic.oup.com/mnras/article/520/1/560/6988185 by University of Sheffield user on 26 May 2023

characterize the structures and underlying physical mechanism(s) which produce the large-amplitude fluctuations in the polarization profile and flocculent features in polar diagrams of strong spectral lines.

The numerical models applied in this study have an effective spatial resolution of ∼600 km s^{-1} for clumps.[16] This is just sufficient to resolve the largest Rayleigh–Taylor instabilities, for example, but already appears to be higher than all SN spectropolarimetry obtained to date. Higher-resolution models to resolve small-scale structures can be achieved with sub-star instead of full-star simulations or, better, a space-domain implementation[17] for our Variable Eddington Tensor solver in HYDRA as discussed by Hristov et al. (2021, and references therein). Investigation of the effects caused by details of the thermonuclear runaway in a $M_{\rm Ch}$ explosion or any secondary C/O ignition would require spectropolarimetry at late times in combination with late-time near- and mid-infrared flux spectra (Hoeflich et al. 2021). Spectropolarimetry will provide a tomographic sampling of the geometric properties of the layer near the Si/Fe interface in the inner regions of the WD remnant, while nebular flux profiles at sufficient spectral resolution will probe the physical conditions and kinematics of this region through unblended line profiles, which are also sensitive to the aspect angle of the observer (Hoeflich et al. 2021). The combination of these two data sets will subject models to critical consistency checks because they investigate the same region from different perspectives. Analogous simulations should be employed to test other models and make use of hydrodynamical simulations to investigate points (e)–(j) in the list above. A detailed discussion of many other scenarios is beyond the scope of this paper. Obviously, similar simulations can be applied to a wide variety of explosion scenarios and other transients (e.g. Leonard et al. 2012; Maund et al. 2019; Buckley et al. 2021; Dessart et al. 2021), and those will be performed in the future.

By using details previously not considered in combination with extensive modelling, we obtained new insights into the formation of p and obtained many results for SN 2019np in Section 5. However, we pushed the analysis to the limit of current data and modelling efforts. This study should be regarded as a pathfinder for a new approach to the analysis of SNe Ia data, to evaluate the limits, and to identify the potential and shortcomings of current observations and theoretical models, to evaluate methods to correct for the ISM, and to develop future polarization programmes (Section 6).

Facilities

The observations were obtained with FORS2 and the VLT at the European Southern Observatory's La Silla Paranal Observatory in Chile. The simulations have been performed on the computer cluster of the astrogroup at Florida State University.

SOFTWARE

IRAF is distributed by the National Optical Astronomy Observatories, which are operated by the Association of Universities for Research in Astronomy, Inc., under cooperative agreement with the National Science Foundation. HYDRA and various modules. OpenDx, an open-source graphics package by IBM.

DATA AVAIBILITY STATEMENT

All data are available on request.

ACKNOWLEDGEMENTS

This study is based on observations collected at the European Southern Observatory under ESO programme 0102.D-0528. We are grateful to the European Organisation for Astronomical Research in the Southern Hemisphere (ESO) for the generous allocation of observing time. We especially thank the staff at Paranal for their proficient and highly motivated support of this project in service mode. PH acknowledges support by the National Science Foundation (NSF) through grant AST-1715133. AVF's SN group at U.C. Berkeley is grateful for financial assistance from the Christopher R. Redlich Fund and many individual donors, including Gary and Cynthia Bengier, Clark and Sharon Winslow, Sanford Robertson, Sunil Nagaraj, Landon Noll, and Sandy Ottelini. The research of YY has also been supported through a Benoziyo Prize Postdoctoral Fellowship.

REFERENCES

Aldering G. et al., 2006, ApJ, 650, 510
Alsabti A. W., Murdin P., 2017, Handbook of Supernovae. Springer International Publishing AG, New York
Anders E., Grevesse N., 1989, Geochim. Cosmochim. Acta, 53, 197
Anderson J. et al., 2018, European Southern Observatory, Doc. No. VLT-MAN-ESO-13100-1543.
Appenzeller I. et al., 1998, Messenger, 94, 1
Arnett W. D., 1982, ApJ, 253, 785
Ashall C. et al., 2021, MIR Spectroscopy of Type Ia Supernovae: The Key to Unlocking their Explosions and Element Production, JWST Proposal. Cycle 1, ID. #2114.
Ashall C. et al., 2022, ApJ, 932, L2
Baron E., Bongard S., Branch D., Hauschildt P. H., 2006, ApJ, 645, 480
Blondin S., Tonry J. L., 2007, ApJ, 666, 1024
Branch D., Falk S. W., McCall M. L., Rybski P., Uomoto A. K., Wills B. J., 1981, ApJ, 244, 780
Buckley D. A. H. et al., 2021, MNRAS, 506, 4621
Bulla M., Sim S. A., Pakmor R., Kromer M., Taubenberger S., Röpke F. K., Hillebrandt W., Seitenzahl I. R., 2016a, MNRAS, 455, 1060
Bulla M. et al., 2016b, MNRAS, 462, 1039
Burke J., Arcavi I., Hiramatsu D., Howell D. A., Mccully C., Valenti S., 2019, Transient Name Server Classification Report, 2019-71, 1
Burke J. et al., 2022, preprint (arXiv:2207.07681)
Chatzopoulos E., Wheeler J. C., Vinko J., 2012, ApJ, 746, 121
Chevalier R. A., Fransson C., 2017, in Alsabti A. W., Murdin P., eds, Handbook of Supernovae. Springer International Publishing AG, New York, p. 875
Cikota A., Patat F., Cikota S., Faran T., 2017, MNRAS, 464, 4146
Cikota A. et al., 2019, MNRAS, 490, 578
Dessart L., Hillier D. J., Blondin S., Khokhlov A., 2014, MNRAS, 441, 3249
Dessart L., Leonard D. C., Hillier D. J., Pignata G., 2021, A&A, 651, A19
Dragulin P., Hoeflich P., 2016, ApJ, 818, 26
Eriguchi Y., Mueller E., 1993, ApJ, 416, 666
Fesen R. A., Höflich P. A., Hamilton A. J. S., Hammell M. C., Gerardy C. L., Khokhlov A. M., Wheeler J. C., 2007, ApJ, 658, 396
Fesen R. A., Höflich P. A., Hamilton A. J. S., 2015, ApJ, 804, 140
Gamezo V. N., Khokhlov A. M., Oran E. S., 2005, ApJ, 623, 337

[16] The effective resolution is estimated from the grid resolution, i.e. the domain size (2 × 25 000 km s^{-1}) divided by the number of grid points (330) in a differential scheme (contributing a factor of ∼2). For spherical clumps as the simplest structures, it is multiplied by another factor 2. This results in 75 km s^{-1} × 2^3.

[17] As part of an ongoing PhD project, the domain deposition is currently being implemented using 'pancake slicing' and cycling between the three Cartesian coordinates.

Downloaded from https://academic.oup.com/mnras/article/520/1/560/6988185 by University of Sheffield user on 26 May 2023

García-Berro E., Lorén-Aguilar P., 2017, in Alsabti A. W., Murdin P., eds, Handbook of Supernovae. Springer International Publishing AG, New York, p. 1237
Gerardy C. L. et al., 2007, ApJ, 661, 995
Hoeflich P., 2017, Explosion Physics of Thermonuclear Supernovae and Their Signatures. Springer Publishing AG, New York, p. 1151
Hoeflich P., Khokhlov A., 1996, ApJ, 457, 500
Hoeflich P., Mueller E., Khokhlov A., 1993, A&A, 268, 570
Hoeflich P., Khokhlov A. M., Wheeler J. C., 1995, ApJ, 444, 831
Hoeflich P. et al., 2017, ApJ, 846, 58
Hoeflich P. et al., 2019, in Formicola A., Junker M., Gialanella L., Imbriani G., eds, Proceedings in Physics, Vol. 219, Nuclei in the Cosmos XV. Springer, New York, p. 187
Hoeflich P. et al., 2021, ApJ, 922, 186
Höflich P., 1991, A&A, 246, 481
Höflich P., 1995a, ApJ, 440, 821
Höflich P., 1995b, ApJ, 440, 821
Höflich P., 1995c, ApJ, 443, 89
Höflich P., 1998, in Mezzacappa A., ed., Proceedings of the 2nd Oak Ridge Symposium on Atomic and Nuclear Astrophysics, Stellar Evolution, Stellar Explosions and Galactic Chemical Evolution. Institute of Physics Publishing, Bristol, UK, p. 693
Höflich P., 2003, in Hubeny I., Mihalas D., Werner K., eds, ASP Conf. Ser. Vol. 288, Stellar Atmosphere Modeling. Astron. Soc. Pac., San Francisco, p. 185
Höflich P., Mueller E., Khokhlov A., 1993, A&A, 268, 570
Höflich P., Khokhlov A., Wang L., 2001, in Wheeler J. C., Martel H., eds, AIP Conf. Ser. Vol. 586, 20th Texas Symposium on Relativistic Astrophysics. Am. Inst. Phys., New York, p. 459
Höflich P., Gerardy C. L., Nomoto K., Motohara K., Fesen R. A., Maeda K., Ohkubo T., Tominaga N., 2004, ApJ, 617, 1258
Höflich P., Gerardy C. L., Marion H., Quimby R., 2006a, New Astron. Rev., 50, 470
Höflich P., Gerardy C. L., Marion H., Quimby R., 2006b, New Astron. Rev., 50, 470
Hosseinzadeh G. et al., 2017, ApJ, 845, L11
Howell D. A., Höflich P., Wang L., Wheeler J. C., 2001, ApJ, 556, 302
Howell D. A. et al., 2005, ApJ, 634, 1190
Hristov B., Hoeflich P., Collins D. C., 2021, ApJ, 923, 210
Hsiao E. Y. et al., 2020, ApJ, 900, 140
Itagaki K., 2019, Trans. Name Server Discov. Rep., 2019-53, 1
Kasen D., 2006, ApJ, 649, 939
Kasen D., 2010, ApJ, 708, 1025
Kasen D., Plewa T., 2005, ApJ, 622, L41
Kasen D. et al., 2003, ApJ, 593, 788
Khokhlov A. M., 1991, A&A, 245, 114
Kilpatrick C. D., Foley R. J., 2019, Astron. Tel., 12375, 1
Kotak R., Meikle W. P. S., Adamson A., Leggett S. K., 2004, MNRAS, 354, L13
Kromer M., Sim S. A., Fink M., Röpke F. K., Seitenzahl I. R., Hillebrandt W., 2010, ApJ, 719, 1067
Kushnir D., Katz B., Dong S., Livne E., Fernández R., 2013, ApJ, 778, L37
Lentz E. J., Baron E., Branch D., Hauschildt P. H., 2001, ApJ, 557, 266
Leonard D. C., Filippenko A. V., 2005, in Turatto M., Benetti S., Zampieri L., Shea W., eds, ASP Conf. Ser. Vol. 342, 1604-2004: Supernovae as Cosmological Lighthouses. Astron. Soc. Pac., San Francisco, p. 330
Leonard D. C., Li W., Filippenko A. V., Foley R. J., Chornock R., 2005, ApJ, 632, 450
Leonard D. C., Dessart L., Hillier D. J., Pignata G., 2012, in Hoffman J. L., Bjorkman J., Whitney B., eds, AIP Conf. Ser. Vol. 1429, Stellar Polarimetry: from Birth to Death. Am. Inst. Phys., New York, p. 204
Livne E., 1990, ApJ, 354, L53
Livne E., 1999, ApJ, 527, L97
Maeda K., Jiang J.-a., Shigeyama T., Doi M., 2018, ApJ, 861, 78
Magee M. R., Maguire K., 2022, MNRAS, 642, 3035
Margutti R. et al., 2014, ApJ, 780, 21
Marietta E., Burrows A., Fryxell B., 2000, ApJS, 128, 615
Maund J. R., Wheeler J. C., Patat F., Baade D., Wang L., Höflich P., 2007, MNRAS, 381, 201
Maund J. R., Wheeler J. C., Baade D., Patat F., Höflich P., Wang L., Clocchiatti A., 2009, ApJ, 705, 1139
Maund J. R. et al., 2010a, ApJ, 722, 1162
Maund J. R. et al., 2010b, ApJ, 725, L167
Maund J. R. et al., 2013, MNRaS, 433, L20
Maund J. R., Steele I., Jermak H., Wheeler J. C., Wiersema K., 2019, MNRAS, 482, 4057
Maund J. R. et al., 2021, MNRAS, 503, 312
Mazzali P. A., Lucy L. B., Danziger I. J., Gouiffes C., Cappellaro E., Turatto M., 1993, A&A, 269, 423
Miller A. A. et al., 2018, ApJ, 852, 100
Moll R., Raskin C., Kasen D., Woosley S. E., 2014, ApJ, 785, 105
Nomoto K., 1982a, ApJ, 253, 798
Nomoto K., 1982b, ApJ, 257, 780
Nomoto K., Sugimoto D., Neo S., 1976, APSS, 39, L37
Nugent P. E. et al., 2011, Nature, 480, 344
Pakmor R., 2017, in Alsabti A. W., Murdin P., eds, Handbook of Supernovae. Springer International Publishing AG, New York, p. 1257
Pakmor R., Kromer M., Taubenberger S., Sim S. A., Röpke F. K., Hillebrandt W., 2012, ApJ, 747, L10
Pakmor R., Kromer M., Taubenberger S., Springel V., 2013, ApJ, 770, L8
Patat F., 2017, in Alsabti A. W., Murdin P., eds, Handbook of Supernovae. Springer International Publishing AG, New York, p. 1017
Patat F., Romaniello M., 2006, PASP, 118, 146
Patat F. et al., 2008, Messenger, 131, 30
Patat F., Baade D., Höflich P., Maund J. R., Wang L., Wheeler J. C., 2009, A&A, 508, 229
Patat F., Höflich P., Baade D., Maund J. R., Wang L., Wheeler J. C., 2012, A&A, 545, A7
Patat F. et al., 2015, A&A, 577, A53
Patra K. C. et al., 2022, MNRAS, 509, 4058
Patterson M. T. et al., 2019, PASP, 131, 018001
Pellegrino C. et al., 2020, ApJ, 897, 159
Penney R., Hoeflich P., 2014, ApJ, 795, 84
Piro A. L., Kollmeier J. A., 2018, ApJ, 855, 103
Piro A. L., Morozova V. S., 2016, ApJ, 826, 96
Quimby R. M., Wheeler J. C., Höflich P., Akerlof C. W., Brown P. J., Rykoff E. S., 2007, ApJ, 666, 1093
Raskin C., Kasen D., Moll R., Schwab J., Woosley S., 2014, ApJ, 788, 75
Reilly E. et al., 2016, MNRAS, 457, 288
Riess A. G. et al., 1999, AJ, 118, 2675
Sai H. et al., 2022, MNRAS, 514, 3541
Serkowski K., Mathewson D. S., Ford V. L., 1975, ApJ, 196, 261
Shen K. J., Moore K., 2014, ApJ, 797, 46
Shen K. J., Bildsten L., Kasen D., Quataert E., 2012, ApJ, 748, 35
Simmons J. F. L., Stewart B. G., 1985, A&A, 142, 100
Stevance H. F. et al., 2019, MNRAS, 485, 102
Telesco C. M. et al., 2015, ApJ, 798, 93
Tody D., 1986, in Crawford D. L., ed., Proc. SPIE Conf. Ser. Vol. 627, Instrumentation in Astronomy VI. SPIE, Bellingham, p. 733
Tody D., 1993, in Hanisch R. J., Brissenden R. J. V., Barnes J., eds, ASP Conf. Ser. Vol. 52, Astronomical Data Analysis Software and Systems II. Astron. Soc. Pac., San Francisco, p. 173
Wang L., Wheeler J. C., 2008, ARAA, 46, 433
Wang L., Wheeler J. C., Höflich P., 1997, ApJ, 476, L27
Wang L., Howell D. A., Höflich P., Wheeler J. C., 2001, ApJ, 550, 1030
Wang L. et al., 2003, ApJ, 591, 1110
Wang L., Baade D., Höflich P., Wheeler J. C., Kawabata K., Khokhlov A., Nomoto K., Patat F., 2006, ApJ, 653, 490
Wang L., Baade D., Patat F., 2007, Science, 315, 212
Woosley S. E., Weaver T. A., 1994, ApJ, 423, 371
Woosley S. E., Weaver T. A., Taam R. E., 1980, in Wheeler J. C., ed., Proceedings of the Texas Workshop, Type I Supernovae. University of Texas, Austin, TX, p. 96
Wu C., Zhang J., Yang Y., Wang X., Huang F., 2019, Transient Name Server Classification Report, 2019-2765, 1

Downloaded from https://academic.oup.com/mnras/article/520/1/560/6988185 by University of Sheffield user on 26 May 2023

Yang Y. et al., 2020, ApJ, 902, 46
Yang Y. et al., 2022, ApJ, 939, 18
Zel'Dovich Y. B., Librovich V. B., Makhviladze G. M., Sivashinskil G. I., 1970, J. Appl. Mech. Tech. Phys., 11, 264

APPENDIX: EXPLOSION TIME OF SN 2019NP

In order to estimate the phases of the FORS2 observations relative to the explosion time of SN 2019np, we modelled the early flux of SN 2019np as a function of time by fitting its *r*-band flux with a power law,

$$f(t) \propto (t - t_0)^m, \tag{A1}$$

where t_0 denotes the time of the first light from the explosion. This formalism assumes that the WD exploded as an expanding fireball with constant temperature and velocity (Riess et al. 1999). The earliest photometric data set of SN 2019np consists of the SDSS *g*- and *r*-band light curves generated by the Zwicky Transient Facility (ZTF) alert packets (Patterson et al. 2019). Owing to the lack of *g*-band photometry at the earliest phases of SN 2019np, we fitted the power law to the *r*-band flux, for which we considered two subsets, namely observations before days ∼−14 and ∼−12, respectively. The fitting is also constrained by the last non-detection on day −18.2. As shown by the filled black and open orange circles in the upper left-hand panel of Fig. A1, after arbitrarily scaling the *g* and *r* light curves of SN 2019np, the evolution of the flux in both bandpasses is consistent between days −15.7 and −12.7, when photometry is available for both filters. The best fit to the observations before day −14 gives $m = 1.20 \pm 0.04$ and a rise time $t_0 = -17.92 \pm 0.06$ d. The statistical error of 0.06 d in t_0 is much smaller than the systematic uncertainty of the time of the *B*-band light-curve maximum, which amounts to ±0.51 d in our analysis and has to be added.

Fig. A1 also compares the flux evolution of SN 2019np to its fit with equation (A1) and includes data for selected other SNe with well-sampled photometry at similarly early phases. The *g*-band light curve of the normal Type Ia SN 2011fe is well approximated by an expanding fireball model (i.e. $m \approx 2$; Nugent et al. 2011). Two cases with an early flux excess, namely SN 2017cbv (Hosseinzadeh et al. 2017) and iPTF16abc (Miller et al. 2018), exhibit a fast rise within the first ∼5 d after the explosion and favour a power-law index around unity. At $m = 1.20 \pm 0.04$, SN 2019np is similar to both of them.

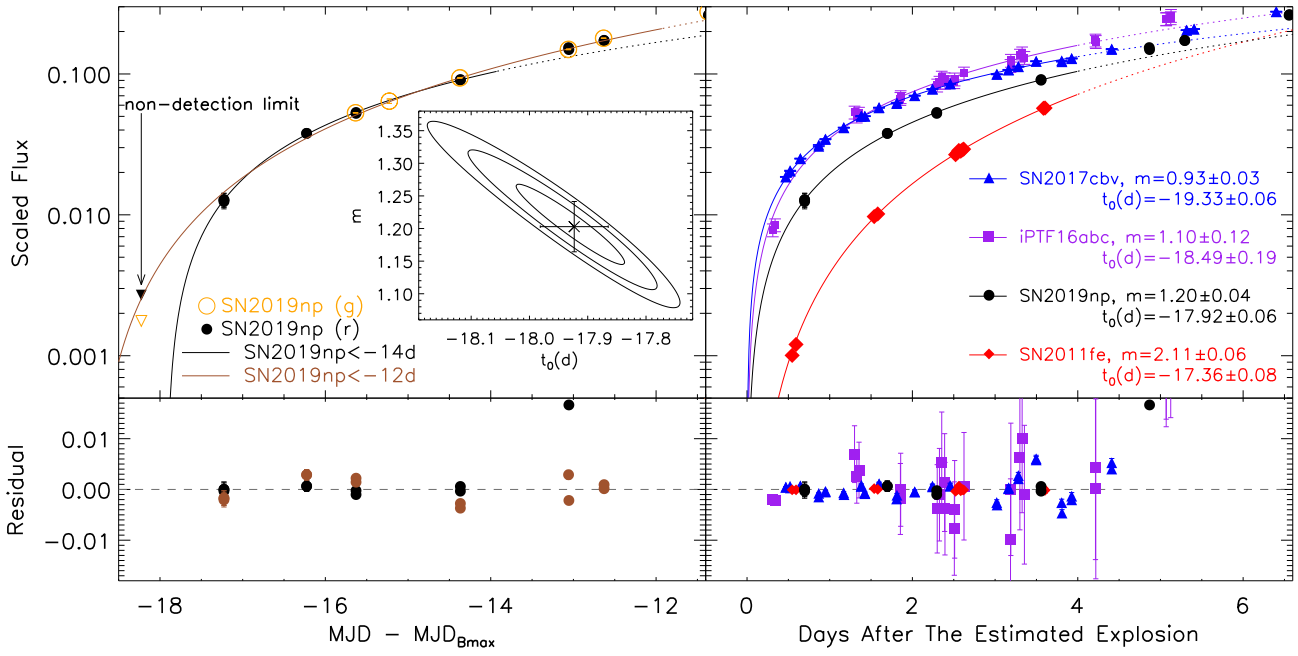

Figure A1. Best-fitting $f \propto (t - t_0)^m$ model to describe the early flux evolution of SN 2019np compared to that of selected other SNe with well-sampled early photometry. All flux distributions are normalized to the peak magnitude measured for each SN in the given bandpasses. In the upper left-hand panel, the black and the brown solid lines fit the *r*-band flux (filled-black circles) of SN 2019np before −14 and −12 d relative to the *B*-band maximum on MJD 58509.7, respectively. In the inset, the inner to outer contours represent the 1σ, 2σ, and 3σ confidence levels of the power-law parameters. The open orange circles mark the *g*-band photometry of SN 2019np. The residuals of the fits to the *r*-band light curves before −14 and −12 d are shown by the black and brown dots, respectively, in the bottom-left panel. The upper-right panel compares the fit of SN 2019np to the *g* light curves of SNe 2017cbv, 2011fe, and iPTF16abc within the first 4 d after explosion. SN 2019np exhibits a similar power-law index as SN 2017cbv and iPTF16abc, for which a blue excess has been identified within the first ∼5 d. The residuals are shown in the bottom-right panel.

This paper has been typeset from a TEX/LATEX file prepared by the author.

Downloaded from https://academic.oup.com/mnras/article/520/1/560/6988185 by University of Sheffield user on 26 May 2023